The Astrophysical Journal, 780:55 (19pp), 2014 January 1 doi:10.1088/0004-637X/780/1/55

FORMATION AND ERUPTION OF AN ACTIVE REGION SIGMOID. I. A STUDY BY NONLINEAR FORCE-FREE FIELD MODELING

Chaowei Jiang[1], S. T. Wu[2], Xueshang Feng[1], and Qiang Hu[2]
[1] SIGMA Weather Group, State Key Laboratory for Space Weather, Center for Space Science and Applied Research, Chinese Academy of Sciences, Beijing 100190, China; cwjiang@spaceweather.ac.cn, fengx@spaceweather.ac.cn
[2] Center for Space Plasma and Aeronomic Research, The University of Alabama in Huntsville, Huntsville, AL 35899, USA; wus@uah.edu, qh0001@uah.edu
Received 2013 June 12; accepted 2013 October 30; published 2013 December 11

ABSTRACT

We present a comprehensive study of the formation and eruption of an active region (AR) sigmoid in AR 11283. To follow the quasi-static evolution of the coronal magnetic field, we reconstruct a time sequence of static fields using a recently developed nonlinear force-free field model constrained by vector magnetograms. A detailed analysis of the fields compared with observations suggests the following scenario for the evolution of the region. Initially, a new bipole emerges into the negative polarity of a preexisting bipolar AR, forming a null-point topology between the two flux systems. A weakly twisted flux rope (FR) is then built up slowly in the embedded core region, largely through flux cancellation, forming a bald patch separatrix surface (BPSS). The FR grows gradually until its axis runs into a torus instability (TI) domain, and the BPSS also develops a full S-shape. The combined effects of the TI-driven expansion of the FR and the line tying at the BP tear the FR into two parts with the upper portion freely expelled and the lower portion remaining behind the postflare arcades. This process dynamically perturbs the BPSS and results in the enhanced heating of the sigmoid and the rope. The accelerated expansion of the upper-portion rope strongly pushes its envelope flux near the null point and triggers breakout reconnection at the null, which further drives the eruption. We discuss the important implications of these results for the formation and disruption of the sigmoid region with an FR.

Key words: magnetohydrodynamics (MHD) – methods: numerical – Sun: corona – Sun: coronal mass ejections (CMEs) – Sun: flares – Sun: magnetic fields

Online-only material: animations, color figures

1. INTRODUCTION

Sigmoid, the name given to forward or inverse S-shaped coronal loops seen often in soft X-ray (SXR) and sometimes in extreme ultraviolet (EUV) emission (Rust & Kumar 1996; Gibson et al. 2002), is one of the most important precursor structures for solar eruptions (Hudson et al. 1998; Canfield et al. 1999, 2007). Thus, it is prudent to concentrate on sigmoidal regions if one wants to understand the structure and evolution of erupting regions due to their higher probability for producing eruptions. This is not surprising as the shape of sigmoids usually indicates sheared and twisted magnetic structures, which carry a field-aligned current and thus free magnetic energy. Most sigmoids appear in active regions (ARs), usually situated on top of a curved polarity inversion line (PIL). They have been envisioned as a twisted and sheared core field, e.g., a magnetic flux rope (FR), embedded in a potential envelope field (Moore & Roumeliotis 1992), which stabilizes the core field against eruption. In morphology, four kinds of sigmoids can be distinguished, i.e., multiple loops, interregion loops, single S-shaped, and double J-shaped loops (Pevtsov 2002). They can also be collectively referred to as two types, transient and long-lived sigmoids, respectively. Transient sigmoids are sharp and bright, and they usually become clearly noticeable only for a short time before the actual eruption, while long-lived sigmoids appear more diffuse and can survive for many hours or even days until the eventual eruption (Green et al. 2007; McKenzie & Canfield 2008). Sigmoids usually evolve into cusps and postflare arcades of loops during eruption, but in some cases they survive and remain even after eruption (Pevtsov 2002; Gibson et al. 2002).

Sigmoids are considered to result from enhanced current dissipation that accumulates hot plasma along correspondingly shaped field lines. Due to the extremely low resistivity of the coronal plasma, these currents need to take the form of thin layers for the resistivity to be important for sufficient dissipation. Narrow current sheets can easily form along magnetic interface layers, e.g., magnetic separatrices and quasi-separatrix layers (QSLs), across which the connectivity of field lines discontinues or changes abruptly (Démoulin 2006, 2007). The interfaces separating a coronal FR from its ambient field usually form the sigmoidal shape when observed from above, and they are naturally invoked in different models of sigmoids (e.g., see review of Gibson et al. 2006). In particular, with an analytical force-free FR model embedded in an arcade field, Titov & Démoulin (1999) showed that in the process of the FR emerging rigidly into the corona, there is a separatrix surface touching the photosphere along sections of the PIL, where the transverse magnetic fields cross from the negative to the positive polarity (opposite to a potential field case). These sections of the PIL are called bald patches (BPs), and the BP separatrix surface (BPSS) has an S-shape viewed from above, which speaks to its potential importance in producing a sigmoid shape. Even in the later phase of emergence, the S-shaped BPSS bifurcates into a double J-shaped QSL with the main body of the FR elevated off the photosphere, the sigmoidal shape remains, which matches the QSL (Aulanier et al. 2010).

Investigations based on numerical simulations have shown that generally a FR does not emerge bodily from below the photosphere, but forms in situ in the corona (Magara 2006; Fan 2009). Nevertheless, those FR-related BPSS and QSL mentioned above are still essential to the FR formation and eruption

processes, since they rely on magnetic reconnections occurring in these thin layers. It has been shown that flux convergence and cancellation yield the formation of a FR through tether-cutting-like reconnection occurring on the photosphere between previously sheared arcades (van Ballegooijen & Martens 1989). This process forms BPs in the PIL, and the sheared field lines reconnect at the BP, pass through the BPSS, and form S-shaped field lines in the rope. With the increase of magnetic pressure in the growing FR, its main body will bulge upward and might detach itself from the photosphere. In such a case, the BPSS bifurcates gradually and transforms into the double J-shaped QSL, the cross section of which contains an X-line-like configuration in the corona, also known as the hyperbolic flux tube (HFT; see Titov et al. 2002). Now the standard tether-cutting reconnection (Moore & Roumeliotis 1992; Moore et al. 2001; Janvier et al. 2013; Liu et al. 2013) settles in, which occurs in the corona at the HFT, as another important mechanism for further building up of the FR from the sheared arcades.

The question of how the eruption of a sigmoidal FR is initiated and driven is still under intense debate (see, e.g., Aulanier et al. 2010; Schmieder et al. 2013; Aulanier 2013, and references therein). In addition to their roles played in the FR formation, both the flux cancellation and tether cutting have also been widely invoked to account for triggering the loss of equilibrium of the FR by increasing the magnetic pressure in the rope and, in turn, reducing the restraining tension force of the envelope field (van Ballegooijen & Martens 1989; Moore et al. 2001; Amari et al. 2003a, 2003b; Linker et al. 2003). However, with a detailed magnetohydrodynamic (MHD) simulation of an eruption initiated in a sheared bipolar region with photospheric field diffusion (emulating the flux cancellation), Aulanier et al. (2010) found that neither of these processes triggers an eruption, but actually, the eruption is caused by a kind of ideal MHD instability of the FR-overlying flux system, i.e., the torus instability (TI; see Kliem & Török 2006). Generally, a coronal FR can be regarded as an anchored partial current ring, which experiences an outward "hoop force" due to the self-repelling force of the image current under the photosphere. This hoop force is counteracted by external potential or sheared field, i.e., the overlaying arcade. The TI describes the instability due to expansion of the FR if the restoring force of the external field decreases with the height faster than the hoop force. This instability can be characterized by a decay index of the external field with an unstable threshold of $\sim$1.5 (Török & Kliem 2007; Aulanier et al. 2010).

Several other models besides the TI have been proposed for the initiation mechanism of the FR eruptions. The kink instability (KI) for a FR occurs if the twist, a measure of the number of windings of the field lines about the rope axis, exceeds a critical value (about 1.5–2), leading to a helical deformation of the FR's axis (Hood & Priest 1981; Velli et al. 1990; Török et al. 2004; Török & Kliem 2005). Numerical models have shown that the KI can generate sigmoidal current sheets just prior to an eruption at the interface of the FR and its ambient field (Kliem et al. 2004; Fan & Gibson 2004), and thus suggests another explanation for transient sigmoids.

The breakout model (Antiochos et al. 1999) provides another possibility for eruptions by directly removing the overlying constraining flux through reconnection above the core field. In the original breakout model based on a quadrupolar magnetic field configuration, the eruption is triggered by reconnection at a coronal null above the sheared core arcade, which removes the overlying flux and then allows the core to escape, similar to the streamer and flux model (Wu & Guo 1997). There are also lateral versions of breakout models proposed (e.g., Chen & Shibata 2000; Lin et al. 2001), in which the coronal null-point reconnection takes place on the side of the eruptive core instead of above it. More complex breakout models have been investigated (e.g., Roussev et al. 2007; Jacobs et al. 2009), which include much more realistic magnetic topology with multiple null points. The critical building block of these models is that the overlying flux contains a coronal null point, which is possibly formed by a new flux emerging into an inverse preexisting field (Wu et al. 2005; Török et al. 2009). It should be noted that although the breakout model generally does not involve a preeruption FR and thus a sigmoid, the breakout reconnection should work for either a sheared arcade or an FR in the core field, as long as there is a null-point existing in the overlying flux.

The aim of this article is to provide a comprehensive study of the whole process of the formation and eruption of a sigmoidal FR and to identify the different mechanisms for the FR built-up and eruption. Our study is based on observations and a nonlinear force-free field (NLFFF) model. Although observations with increasing resolutions have shed important light on this process (e.g., Schmieder & Aulanier 2012; Zhang et al. 2012; Cheng et al. 2013; Li & Zhang 2013a, 2013b), the critical parameter, i.e., the coronal field, is difficult to measure at least at present. NLFFF extrapolation has been accepted as a viable tool to obtain the preeruption, near-static coronal field due to the low-β (ratio of plasma pressure to magnetic pressure) nature of the corona (Schrijver et al. 2008; Wiegelmann 2008; Savcheva & van Ballegooijen 2009; Su et al. 2011). Based on a time sequence of static force-free fields, one can further study the slow build-up process of the field prior to eruption by assuming that such evolution can be described by successive equilibria (Régnier & Canfield 2006; Wu et al. 2009; Jiang et al. 2012a; Sun et al. 2012). This method is justified by the fact that the evolution of the coronal field, driven by the photospheric motion with a flow speed less than several km s^{-1}, is sufficiently slow compared with the speed for the coronal field relaxing to equilibrium (i.e., the coronal Alfvén speed), which is up to thousands of km s^{-1} (Antiochos 1987; Seehafer 1994). Although the dynamic evolution of the field intrinsically requires an MHD simulation driven by photospheric fields and flows, such a data-driven simulation (Wu et al. 2004, 2006) is generally prohibitive in this type of study due to the very long time of slow evolution and very high Alfvén speed in the corona, which is difficult to handle in numerical schemes (Jiang et al. 2012a). Thus it is more practical to use the successive extrapolated fields to compare with an idealized MHD simulation for our purpose, as was done by Savcheva et al. (2012a).

The studied event is the formation of a sigmoidal FR in AR 11283 from 2011 September 4 to 6 and its eruption. As shown in the following, this event involves a variety of magnetic processes including flux emergence, flux cancellation, ideal MHD instability, and breakout reconnection. It thus provides an attractive sample for our study. We present an NLFFF model to study the slow evolution of the magnetic field of the region over three days leading to an X-class flare on 2011 September 6. Our attention is focused on the building-up process of the magnetic topology and nonpotentiality of the preeruption field and the initiation mechanism of the eruption. In Section 2, relevant observations of AR 11283 during the time of our interest is described briefly. We then analyze the magnetic evolution prior to and through the sigmoid eruption for the photospheric field

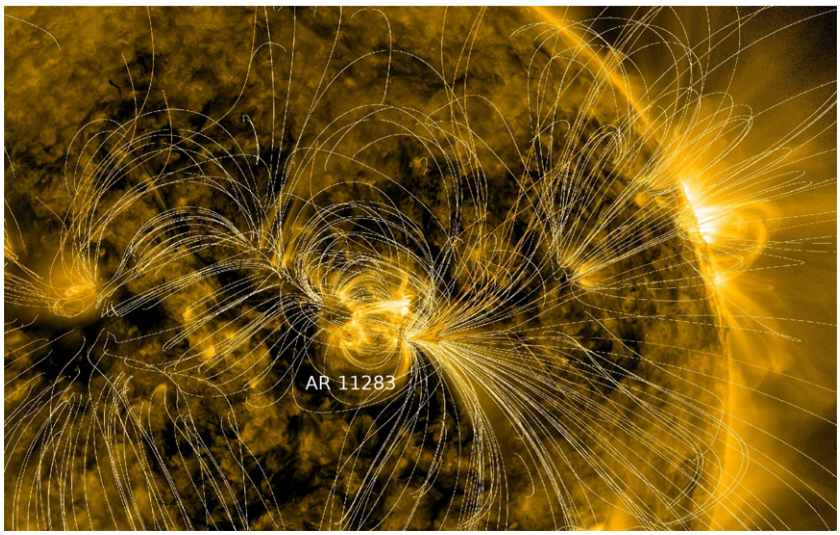

Figure 1. Part of a full-disk *SDO*/AIA-171 image taken at the end of 2011 September 6. Overlying is the PFSS (potential field source surface) field lines to show the large-scale magnetic environment of AR 11283.

(A color version of this figure is available in the online journal.)

in Section 3, and for the coronal field in Section 4, based on the *SDO*/Helioseismic and Magnetic Imager (HMI) magnetograms and our NLFFF model. In Section 5 we study the initiation mechanism of the eruption. Section 6 is devoted to the analysis of the evolution of magnetic energy. The dynamic evolution of the field during eruption cannot be reproduced by the static extrapolation and strongly requires an MHD simulation (Jiang et al. 2013; Kliem et al. 2013).[3] In the second article of this series, we will conduct a full MHD simulation and a detailed analysis of the fast magnetic evolution during the sigmoid eruption.

2. OBSERVATIONS

AR 11283 is one of the very productive ARs in the new solar cycle. It has produced several major flares/coronal mass ejections (CMEs) when near the disk center from 2011 September 5 to 7. Figure 1 shows the AR's location on the disk on September 6. Potential field lines overlaid on the AIA-171 image illustrate the large-scale magnetic environment of the AR. We study the evolution of this region from September 4 to 6. Figure 2 gives the evolution of the photospheric magnetic flux distribution observed by *SDO*/HMI. Initially, on September 4, this region has a simple bipolar configuration as a mature AR, with a leading negative-polarity sunspot N0 and a following positive-polarity P0 that appears much more dispersed. Evolution of the photospheric field is then dominated by a new bipole (labeled as P1/N1) emerging into the west of the preexisting negative polarity N0, forming a delta sunspot group. The new polarities move apart from each other quickly, as usually observed in flux emergence site, and N1 progressively approaches the west boundary of the magnetogram. Note that the positive P1 is surrounded by negative flux, indicating that a coronal null point is likely formed above. After the initial stage of flux emergence with the apparent new flux injection finished, rotation of P1 and shearing motion between P1/N0 are observed. Such photospheric motions make a continuous injection of magnetic free energy and helicity into the corona. Meanwhile, cancellation of flux elements with inverse polarities along the PIL can be clearly seen by inspecting the animation of Figure 2.

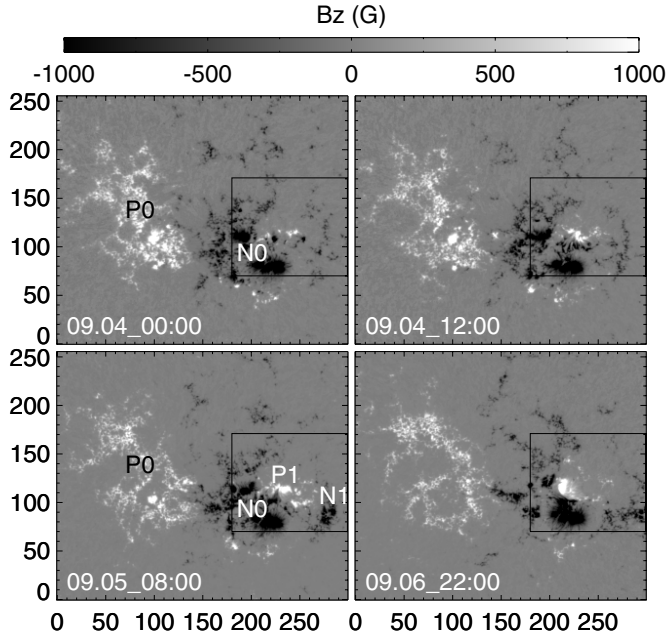

Figure 2. Evolution of the photospheric field. The black boxes outline the region of the flux emergence and eruption. P0/N0 label the preexisting polarities, and P1/N1 label the new emerging polarities. The length unit is arcsec.

(An animation of this figure is available in the online journal.)

Figure 3 shows the evolution of the EUV emissions observed by *SDO*/AIA, which also reflects well the emergence process. Roughly outlined by the enhanced emission, the basic magnetic topology evolves from a single field-line connectivity domain of P0–N0 (excluding some outer loops possibly connecting to surrounding ARs) to two domains of different connectivity. The new domain appears to be embedded in the preexisting one. The separatrix of the two connectivity domains manifests itself rather clearly in the AIA-335 images (denoted by the boxes in Figure 3), showing roughly a closed circular shape expanding with time. During the emergence process, small flares and jet-like features are frequently observed, which is

[3] A preliminary MHD simulation of this eruption process has been carried out by Jiang et al. (2013).

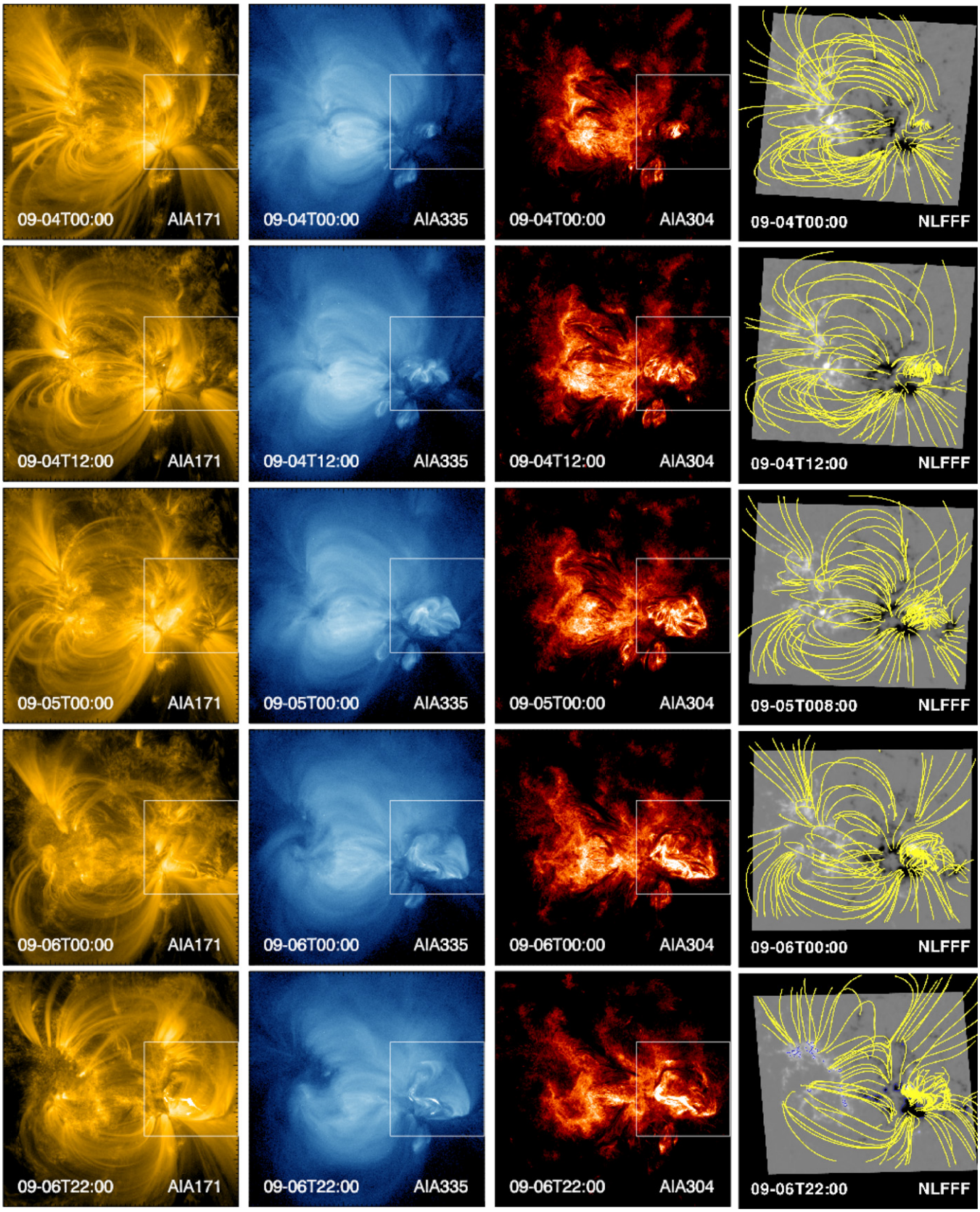

Figure 3. Evolution of the AR observed in different AIA channels and modeled by NLFFF extrapolations (yellow lines are the magnetic field lines and B_z is shown at the bottom). The boxes outline the flux emergence site. View angles of the NLFFFs are aligned with the AIA images.

(An animation and a color version of this figure are available in the online journal.)

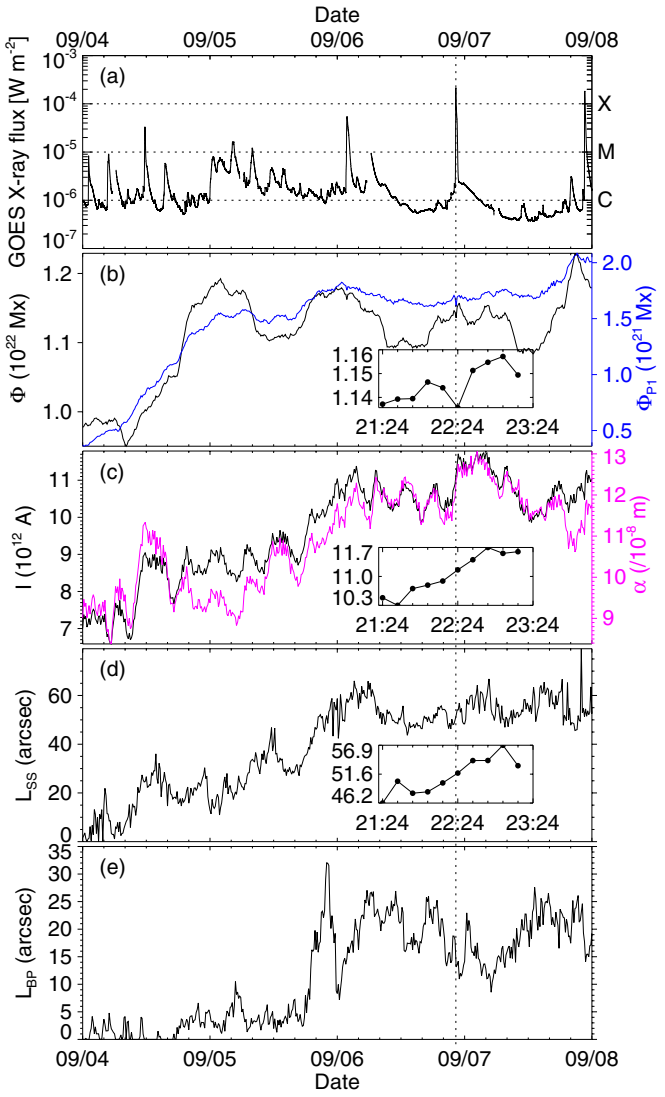

Figure 4. Evolution of different parameters over four days. (a) *GOES* soft-X ray flux (1–8 Å channel). (b) Total unsigned magnetic flux Φ and the new emerging positive flux Φ_{P1}. (c) Total unsigned current I and the torsion parameter α. (d) Length of strong sheared PIL: L_{SS}. (e) Length of BP on the main PIL: L_{BP}. The vertical dashed lines indicate the peak time of the X2.1 flare at 22:20 UT on September 6. Insets of (b), (c), and (d) show results with 2 hr around the flare peak time.

(A color version of this figure is available in the online journal.)

likely due to reconnection accounting for the coronal field reconfiguration. The flares also demonstrate circular ribbons outlining the magnetic separatrix, which strongly implies the presence of a fan-spine topology associated with a coronal null (Masson et al. 2009; Wang & Liu 2012; Jiang et al. 2013; Sun et al. 2013). The embedded core field is significantly sheared on September 6, and by the end of the day, S-shaped loops appear progressively from the highly sheared arcades above the PIL.

The most powerful eruption occurs in the embedded region near the end of September 6. An X2.1 flare starts at 22:12 UT, peaks at 22:20 UT, and ends at 22:24 UT, as shown by the *GOES* flux in Figure 4(a). The flare ribbons consist of two different components, an enhanced circular ribbon at the same location of the magnetic separatrix around the new emerged core, and a standard flare ribbon along the main PIL between P1/N0 (Jiang et al. 2013; Dai et al. 2013). A remarkable S-shaped sigmoid brightens a few minutes before the flare, followed by a drastic eruption of FR and an associated filament toward the northwest that evolves into a CME (Feng et al. 2013; Jiang et al. 2013). Significant movement of the filament persists until the end of the day. The sigmoidal field reforms shortly after this eruption, and another X1.8 flare occurs at the same site on the following day, with a similar preflare sigmoid observed. Our study is focused on the magnetic field evolution leading to the sigmoid eruption event on September 6.

In the following sections we analyze the long-term magnetic evolution prior to the eruption to show how the nonpotentiality accumulates and the sigmoidal field forms. Attention is also paid to the abrupt change of the field across the major flare. The investigation is performed first for the photospheric field and then for the three-dimensional (3D) coronal field.

3. EVOLUTION OF THE PHOTOSPHERIC FIELD

Based on the vector magnetograms observed by *SDO*/HMI[4] with a cadence of 12 minutes, we plot the evolution of a set of parameters in Figure 4, including the total unsigned flux $\Phi = \int_S |B_z| ds$ (where S represents the photosphere) and the unsigned current $I = \int_S |j_z| ds$, the torsion parameter $\alpha = \mu I/\Phi$, and the length of the strong sheared PIL, L_{SS}, which is defined as the portions of the main PIL with the shear angle $>45^\circ$ and the transverse field >300 G (Falconer et al. 2002; Wu et al. 2009). We focus on the field in the emergence/eruption region outlined by the black box on the magnetograms in Figure 2. The current distributions and the locations of the strong sheared PIL are overlaid on the vector magnetograms as shown in Figure 5.

As shown in Figure 4(b), the total magnetic flux increases mainly on the first day and then decreases episodically and slightly because of the combined effects of flux emergence and cancellation. We also compute the flux of the new emerging P1, Φ_{P1}, which is a more suitable monitor for the flux emergence. Φ_{P1} increases fast on the first day, climbing from $\sim$0.3 to $\sim 1.5 \times 10^{21}$ Mx and shows no significant increase afterward. Although interrupted repeatedly by small flares, the nonpotentiality parameters, i.e., the total current I, field twist α, and magnetic shear L_{SS} (panels (c) and (d) of Figure 4) show an evolution trend of continuous increasing until September 6. While the flux emergence is dominant on the first day, the most significant increase of the nonpotentiality occurs on the second day (September 5), during which the photospheric shear and rotation are most clearly observed (Figure 5). This demonstrates that the successive accumulation of nonpotentiality is mainly due to the surface motion (shear/twist) on the photosphere but not the flux emergence.

We do not find a distinct decrease of the photospheric nonpotentiality parameters through the major flare (see the insets in panels (c) and (d) of Figure 4 for the 2 hr evolution around the flare peak time). On the contrary, they increase slightly, which is possibly a result of the so-called implosion effect on the photosphere by the eruption (Hudson 2000), which enhances the transverse field and holds the magnetic stress (associated with photospheric magnetic shear) during the flare (e.g., Wang et al. 2012; Liu et al. 2012; Wang et al. 2013). Inspection of Figure 5 shows that the transverse field near the PIL indeed increases from 22:00 UT to 22:36 UT. A study of the photospheric abrupt change during this flare has been

[4] The data is downloaded from the Web site http://jsoc.stanford.edu/jsocwiki/ReleaseNotes2, where products of HMI vector magnetic field data are released for several ARs.

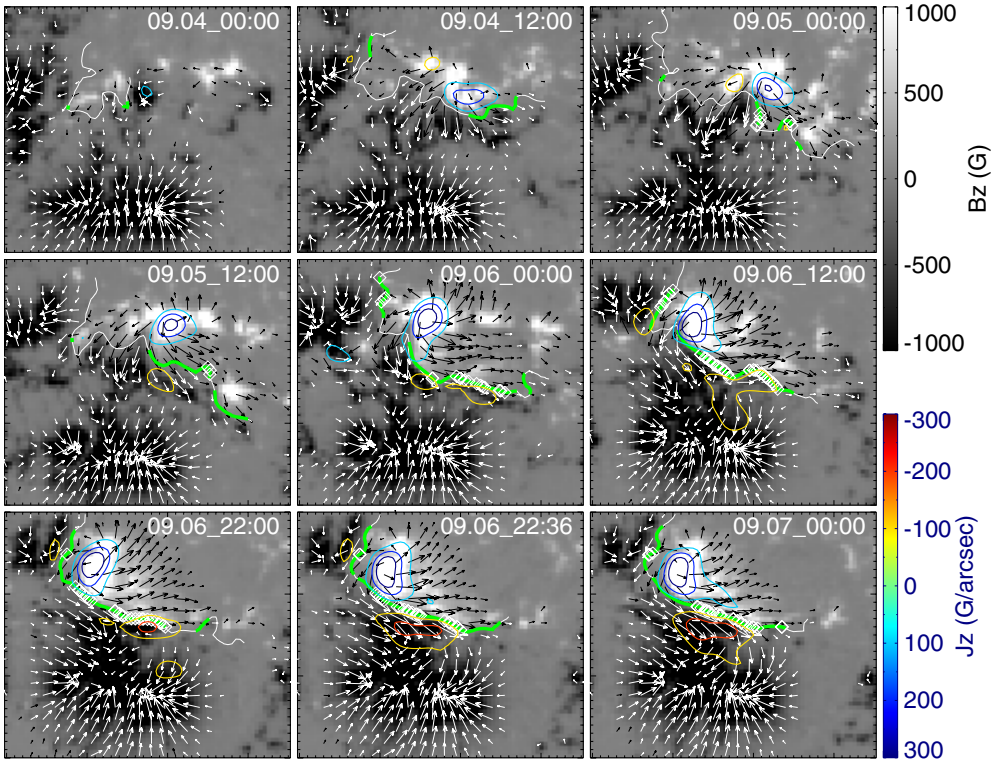

Figure 5. Evolution of the photospheric vector field in the core region. The vectors represent the transverse field (above 200 G), with the longest vector as 1700 G. Colored, closed contour lines represent the vertical current density J_z derived from 5 pixel Gaussian-smoothed vector magnetogram. The white lines indicate the main PIL and the thick green segments denote the strong magnetic shear (shear angle $>45^\circ$) parts with strong transverse fields (>300 G). The length of these parts of the main PIL is L_{SS}. The white diamonds overlaid on the PIL represent the locations of BP.

(A color version of this figure is available in the online journal.)

carefully performed by Petrie (2012), and the same conclusion was drawn. As a consequence, it might be difficult to capture the features of releasing nonpotentiality during the flare solely in the photospheric field, thus a point of view from the 3D coronal field is required. The enhanced transverse field suggests a shortening of the core field lines (possibly due to the flare-related reconnection). This is confirmed by the rapid change of the vertical current distribution during the flare. As shown in Figure 5, prior to the eruption a pair of reversed strong current concentrations are located beside the main PIL, and they approach much closer after the flare. According to the near force-free assumption that coronal currents follow along field lines, there should be field lines (possibly a sheared FR) connecting the pair of current concentrations, and their coming together naturally indicates a shortening of the field lines connecting them.

Based on the vector magnetogram, we can find the BPs on the main PIL where the transverse fields cross the PIL from negative to positive flux. Since the photosphere can be regarded as a line-tying boundary for the coronal field, a BP field line is thus very special because it is anchored at the BP in addition to its two footpoints. As a result, the continuous set of BP field lines forms a BPSS and divides the coronal field into different topological domains. Thus finding the locations of BP is important to study the magnetic topology of the coronal field. Furthermore, the BP is usually an indicator of the presence of FR in the corona (Titov & Démoulin 1999; Aulanier et al. 2010) and thus is essential in the studied event. We compute the BP locations according to the condition $\mathbf{B} \cdot \nabla B_z > 0$ on the main PIL and plot them in Figure 5. We also plot the time evolution of the total length of the BPs, L_{BP}, in Figure 4(e). The plots show that extended BPs appear and develop on the central portion of the main PIL after about 12:00 UT on September 5, a half-day later than the beginning of substantial increasing of the strong shear length L_{SS}. Within hours, the BP length grows to more than half of the L_{SS}. It shrinks slightly through the eruption but never disappears. Due to the weak twisting of the related FR, the BP is usually broken into several segments. We study the BP evolution further in the following section, along with relevant coronal fields.

4. DEVELOPMENT OF THE CORONAL FIELD

4.1. Field Extrapolation Method

In the duration without dynamic eruptions, the coronal field evolution can be regarded as quasi-static and can be modeled well by the NLFFF model. The basic assumption of the NLFFF model is that the Lorentz force is self-balancing in the corona because of its low-β environment. To solve the general NLFFF problem

$$(\nabla \times \mathbf{B}) \times \mathbf{B} = \mathbf{0}, \quad \nabla \cdot \mathbf{B} = 0, \tag{1}$$

we have developed an MHD-relaxation-based code, CESE–MHD–NLFFF (Jiang & Feng 2013). We start from a potential field based on the normal component of the magnetogram, then replace the field at the bottom boundary with the vector magnetogram and use a zero-β MHD relaxation technique to achieve the final force-free state. To improve the convergence speed of the MHD relaxation, we employ an advanced conservation-element/solution-element (CESE) space-time scheme implemented on a block-structured, nonuniform adaptive grid with parallel computation (Jiang et al. 2010). For a detailed description of the CESE–MHD–NLFFF code please refer to Jiang et al. (2011) and Jiang & Feng (2012, 2013).

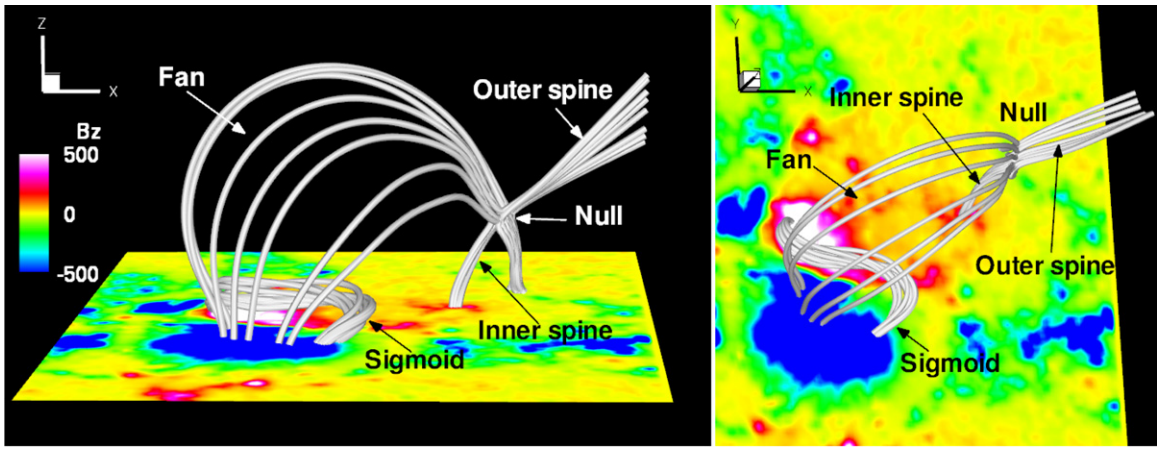

Figure 6. Magnetic topology based on NLFFF extrapolation for the preeruption field at 22:00 UT on September 6. The sigmoid field is represented by the low-lying S-shaped lines; field lines closely touching the null outline the spine-fan topology of the null, at which the lines form an X-point configuration. The null point is situated at about 18 arcsec (13 Mm) above the photosphere and 50 arcsec away from the sigmoid in the same direction of the eruption. The left panel is a side view, and the right panel is the *SDO* view.

(A color version of this figure is available in the online journal.)

Since the photospheric field contains force (due to high-β) and measurement noise, a new preprocessing code (Jiang & Feng 2014) is applied to remove the force and smooth the raw data, which provides a more consistent magnetogram for the NLFFF model. In our extrapolation, we first preprocess the raw magnetograms with their original resolution (i.e., 0.5 arcsec) and then rebin them to 1 arcsec pixel^{-1} as the final input for the extrapolation code. The field of view (FoV) of the vector magnetograms is 300×256 arcsec^2. To reduce the numerical boundary influence, we use a larger extrapolation box of $448 \times 384 \times 320$ arcsec^3, which includes a peripheral region of 64 arcsec width around the vector magnetogram, and the side and top boundaries of this larger extrapolation box are fixed with the potential field value during the relaxation process.

For the long-term evolution of four days, we extrapolate the fields with a cadence of 4 hr. For the 2 hr around the X2.1 flare (from 21:24 UT to 23:24 UT on September 6) extrapolation is performed for the full 12 minute cadence. In Figure 3, the 3D field lines are plotted for five snapshots before the eruption. Comparison with the AIA-171 loops shows that the field lines resemble well the coronal loops in each time, demonstrating the validation of using the NLFFF model to reproduce the slow evolution of the coronal field. There are also some large loops not reconstructed well, and these loops are closed connecting to the northwest of the AR, which is out of the magnetogram's FoV (see the larger FoV image in Figure 1). Such misalignment between extrapolation and observation results from the flux imbalance of the vector magnetogram, which has an average value of -10% (Jiang & Feng 2013), and a spherical extrapolation with a larger magnetogram would be better for these long-connecting loops (Jiang et al. 2012b; Savcheva et al. 2012b). Nevertheless, Jiang & Feng (2013) have demonstrated that the current code can reconstruct the AR's core field excellently (e.g., the flux emergence site here).

4.2. Basic Magnetic Configuration

Figure 6 shows the basic configuration of the preeruption field. It reveals that a sigmoidal field is embedded in a typical spine-fan topology of a coronal null-point above P1. The magnetic null is located in the northwest (the direction of the eruption) of the sigmoid at a height of 13 Mm. In the figure we plot several representative field lines touching the null, which form a remarkable X-point configuration at the null. Field lines going through the null are of two types called spine and fan; the spine consists of two singular field lines, the inner and outer spines, belonging to two different connectivity domains that are divided by a dome-shaped separatrix surface formed by the fan lines (compare Figure 1 of Pariat et al. 2009 who gave an idealized model of null topology). Naturally, the fan surface intersects with the chromosphere in a closed circle. The circular flare ribbon is evidence of the reconnection occurring at the null and is produced by reconnection-accelerated particles along the fan lines down to the chromosphere. The outer spine extends to the northwest, and it appears to be closed connecting out of the extrapolation box, as shown by the large-scale field lines in Figure 1. The corresponding remote brightening at the outer spine footprint is observed in the northwest of the AR (with a distance of roughly 200 arcsec) at about 22:23 UT, almost at the same time as the appearance of the circular ribbon. We note that there are also possibly some field lines around the outer spine connected to P0, as another remote ribbon appears at P0 near the flare peak time (Dai et al. 2013).

In Figure 7, we plot the evolution of a vertical cross section of the field to show the formation of the basic topology. The null topology on the two-dimensional (2D) slice displays an X-point configuration. As P1 emerges, the null forms and lifts up as the field lines expand, along with successive expansion of the dome-like fan domain. In this domain the field lines connect P1 to N0, and out of the domain the field lines connect N0 to P0 or positive polarities out of the FoV, while N1 merges with N0. In this process, small reconnections at the null account for the connectivity interchange between field lines in and out of the closed fan domain. This reconnection usually manifests itself by small flares with a circular shape tracking the chromospheric footpoints of the fan lines. This basic magnetic topology forms at the end of the first day while the field is still near potential (also see Section 6 for an analysis of the volume energy). After that a FR forms gradually above the main PIL of P1/N0, as indicated by the spiral of the 2D-projection field lines, which are a manifestation of the poloidal flux in the rope. Approaching the eruption, the 2D spiral expands greatly along with an increase of the current, as more and more flux is transferred into the rope. In Figure 7, a distinct variation of J/B (i.e., the

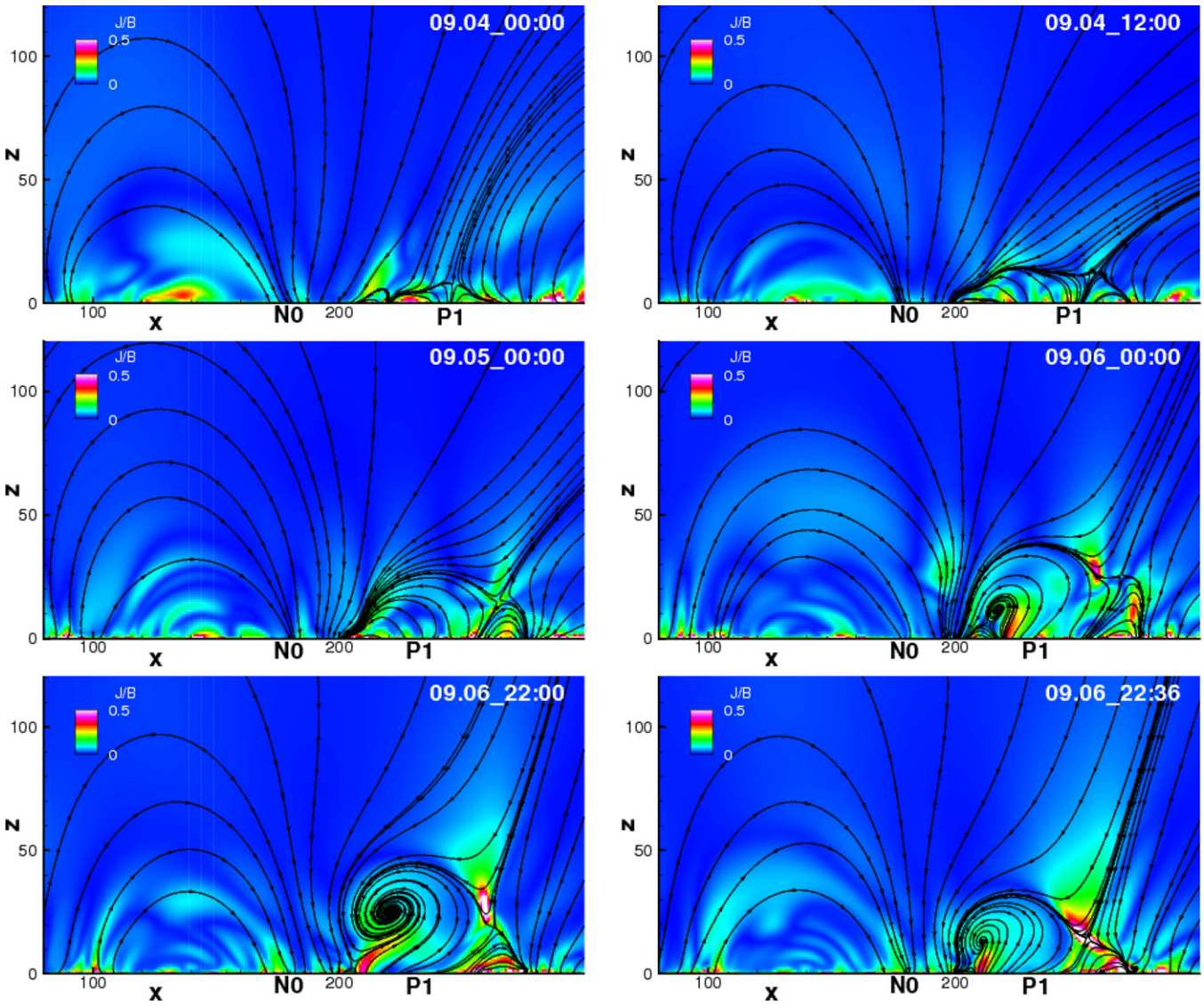

Figure 7. Evolution of vertical slice data ($y = 115$) from the 3D NLFFF volume. We choose slices passing through the main polarities (P0, N0, and P1) for outlining the temporal evolution of the basic magnetic topology. The black lines with arrows are field-line tracings of the magnetic components (B_x, B_z) on the x–z plane, thus they do not necessarily show the 3D field-line connectivity. Colored images of J/B are plotted to show roughly the locations of magnetic separatrices and QSLs.
(A color version of this figure is available in the online journal.)

currents normalized by magnetic field strength) can be seen around the spiral flux. As shown by Savcheva et al. (2012a, 2012b) and (Aulanier et al. 2010) such current concentrations match the main QSL that separates the FR from its surroundings.

Although the magnetic field is reconstructed statically, the successive results vividly reproduce the emerging process. It is worth noting that Figure 7 shows the field constrained by data and not the theoretical models of flux emergence shown in previous works (e.g., Shibata 1998).

4.3. The Core Field

Using an idealized numerical simulation, Aulanier et al. (2010) showed that in a sheared bipolar region the building-up of an FR begins with the appearance of BP. In this event, the BP appears first at about 12:00 UT, September 5. In Figure 8, we plot four snapshots of the buildup process of the FR and a snapshot after its eruption. The magnetic field lines are compared with the observations in a high-temperature channel (AIA-335, 2.5 MK) and a low-temperature channel (AIA-304, 0.05 MK). In the magnetic field plots, the yellow lines are traced through the BP (red parts of the PIL), forming the BPSS; the cyan lines represent some sample field lines closely above the BPSS. The integrations of the current density $J = |\nabla \times \mathbf{B}|$ along z (approximately in the line-of-sight (LoS)) are plotted to show the main body of the FR. We note that in the corona, besides the volume currents, currents also develop in the form of thin sheets along the BPSS and other separatrix and QSL, but these current sheets ought to be very thin and beyond our grid resolution. Furthermore these current sheets form only in the presence of footpoint motions, thus it is difficult to recover them by a static extrapolation model (Savcheva et al. 2012b). As a result, in our model, only the FR's volume currents contribute to the LoS integrated currents. In Figure 9 we further plot a vertical slice of the NLFFF data for each snapshot (the locations of these cuts are overlaid on the plots of the LoS integrated currents in Figure 8). These slices are cut through the middle of the current concentrations in a direction perpendicular to the central PIL, thus corresponding to the central cross sections of the developing FR. In these cross sections, as in Figure 7, the poloidal flux of

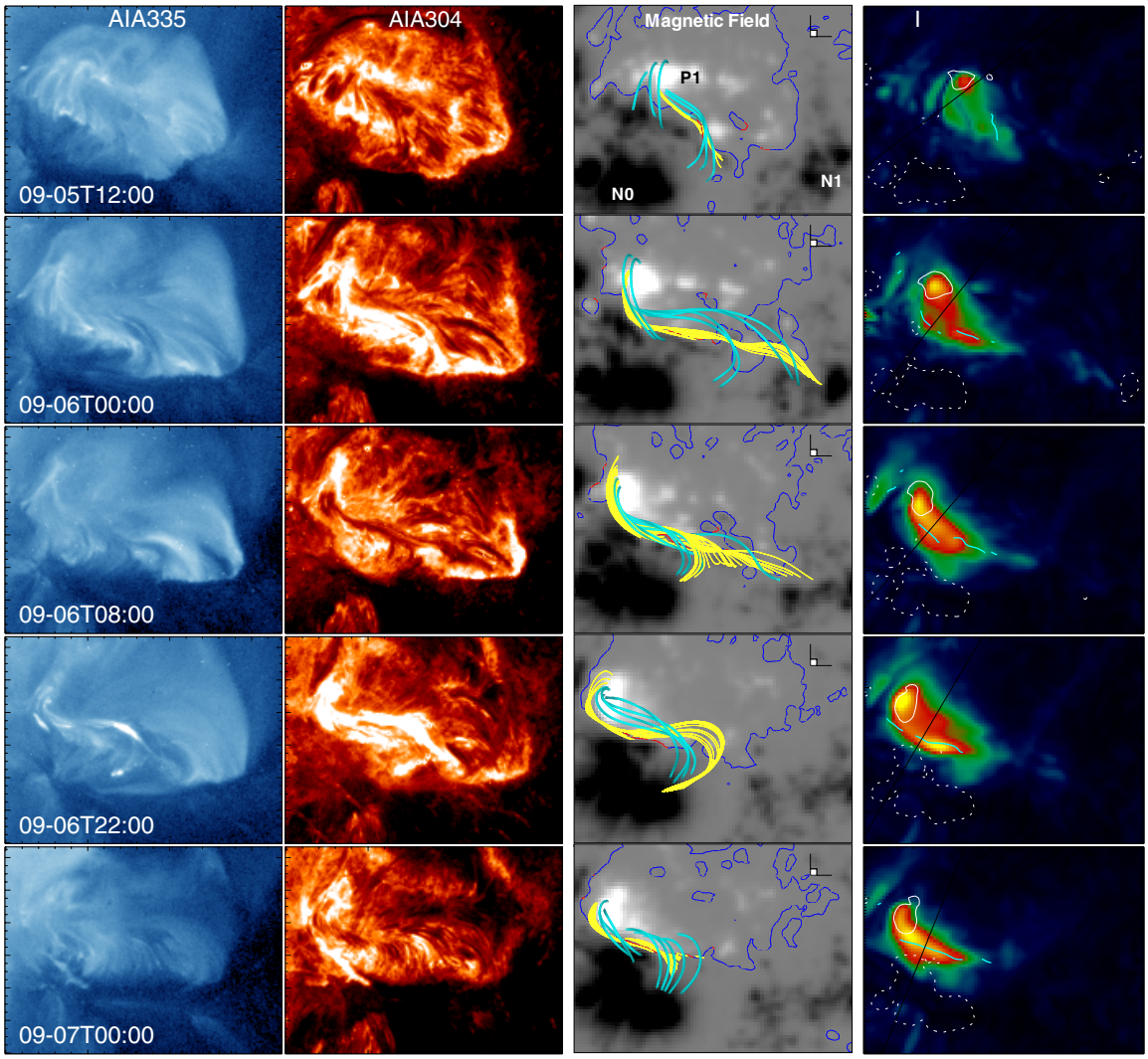

Figure 8. Evolution of the core field. Plots from left to right are, respectively, AIA-335 and AIA-304 images, sample coronal field lines, and the LoS integrated current. In the magnetic field plots, the blue contour lines indicate the PIL, and the red portions denote the BPs; field lines in yellow are traced through the BPs, forming the BPSS; the cyan lines represent some sample field lines closely above the BPSS. In the plots of integrated currents, brighter colors indicate more intense currents; the contour lines represent the B_z of ± 1000 G; the cyan segments indicate the BPs; and the black lines denote the locations where we slice the central cross sections of the FR.

(A color version of this figure is available in the online journal.)

the FR forms a helical shape, and the helical center can be regarded as the apex of the FR axis. In Figure 9 we also show the distribution of J/B, which can help us identify sites of possible magnetic separatrices and QSLs (e.g., Fan & Gibson 2007; Pariat et al. 2009). As shown in the plots, J/B roughly enhances the boundary of the rope and its ambient flux, i.e., the BPSS.

It is interesting to find that the EUV structures are matched very well by the BPSS and nearby field lines rather than by the LoS integrated currents (i.e., the FR's main body). As can be seen, the hot structures and the cold filaments are cospatial with each other and are both represented well by the BPSS field lines. The reasons are twofold: on the one hand, as aforementioned, BPSS are preferential sites where thin sheets of currents form due to persistent photospheric motion. Reconnection occurs continuously at the BPSS and produces the high-temperature emission. The volume currents in the FR, although strong, are extended, thus its dissipation is much slower than those BPSS currents and produce no enhanced emission. As a result, the hot emission mainly corresponds to the BPSS and related field lines. For the same reason, high-temperature EUV emissions are also enhanced along the fan separatrix of the null point, making the separatrix rather clear in its evolution (see Figure 3). On the other hand, the BPs are places where field lines are tangential to the photosphere and thus concave upward. Thus, the field lines just above the BPs form dips where the filament matter can be sustained, which explains why the filaments seen in AIA-304 are closely cospatial with the BPs (e.g., Aulanier et al. 1998).

The BPSS field lines coincide well with the sigmoid. In Figure 10, as an example, we plot a set of BPSS field lines (the thick white lines) and overlay them on the AIA-94 image of 22:00 UT, September 6, when the sigmoid structure was observed most clearly just prior to its eruption. The sigmoid has a thin and enhanced forward-S shape (indicating a right-hand twist) in the AIA-94 wavelength (6.3 MK) and is also well shaped but more diffuse in SXR taken by *Hinode*/XRT. Perfect alignment of the BPSS field lines in the S-shape of the sigmoid can be seen. We also plot field lines near the axis of the FR (the

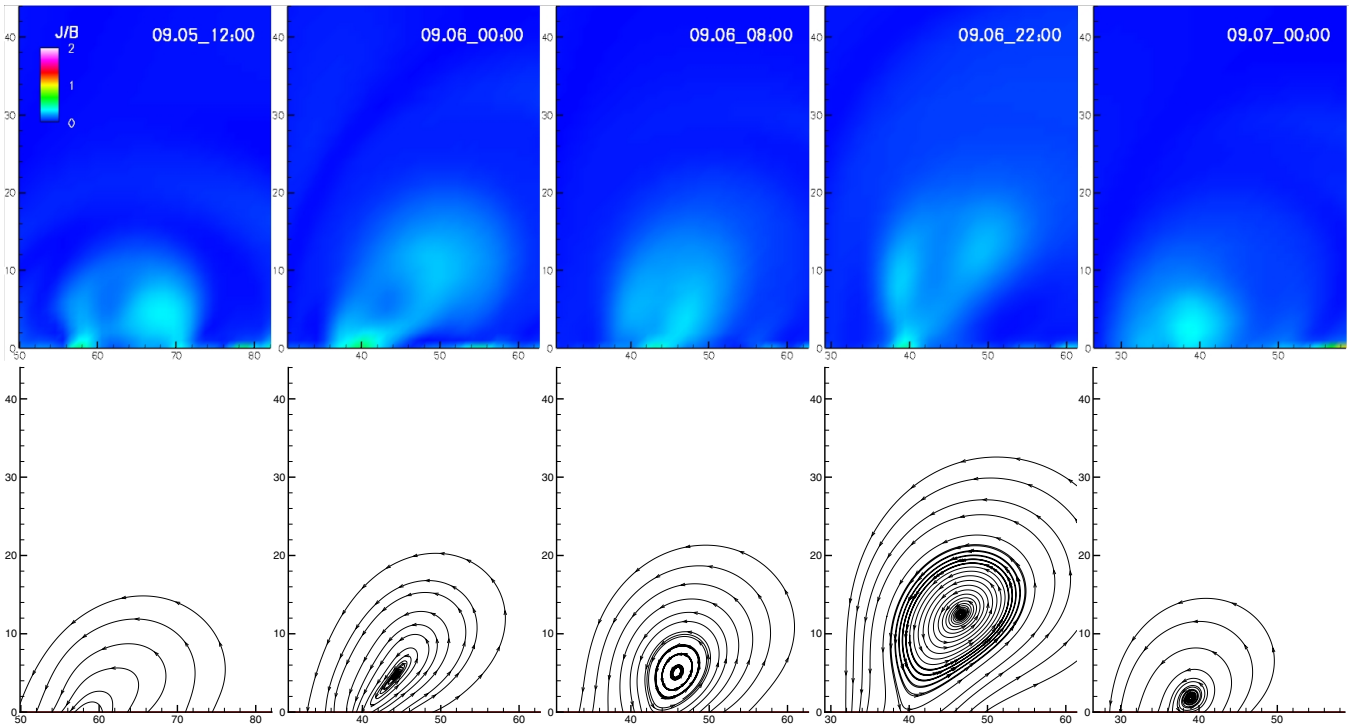

Figure 9. Evolution of the central cross section of the FR. Locations of these slices are denoted by the black lines in the last column of Figure 8. The top panels show currents normalized by the field strength, and the bottom panels show the field-line tracing of the poloidal flux of the FR, which forms helical field lines centered at the axis of the FR.

(A color version of this figure is available in the online journal.)

thick colored lines) to compare its inner body with the sigmoid. These field lines are weakly twisted and also exhibit a slight S-shape, but they clearly do not match the sigmoidal emission in either location or shape. Although we cannot recover the BPSS current sheet here, MHD simulation indeed shows that current sheet spontaneously develops along the BPSS once the coronal field is driven by photospheric motions (Pariat et al. 2009; Aulanier et al. 2010). This supports the BPSS model for this sigmoid in that the current sheet forming along the sigmoid-shaped BPSS produces the enhanced emission of the EUV and SXR sigmoid (Titov & Démoulin 1999; Gibson et al. 2004, 2006; McKenzie & Canfield 2008).

4.4. Formation of the Flux Rope

Following the time evolution of the magnetic field, we see a transition of the initial potential arcade to a double-J-shaped sheared arcade and further to an S-shaped FR, along with the increasing of the volume current. This process is driven by the diverging motion between P1 and N1, the shearing motion between P1 and N0, and the rotation of P1. Clearly the FR does not emerge bodily with magnetic flux from below the photosphere but is built up in the corona by a combination of different kinds of magnetic reconnections, which is discussed below. In Figure 11 we select field lines in the static model to illustrate these reconnection processes. Although these plots do not represent the dynamic evolution of field lines during reconnections, they help us understand how the field-line connectivity is changed by the reconnections.

As shown in Figure 8 from 00:00 UT to 22:00 UT on September 6, some very long arcades (including some field lines in the BPSS) connecting P1 and N1 develop J-shaped lines as their south footpoints slip from N1 to N0. Such transformation can be attributed to the slipping type of reconnection, in which the field line changes its connection quickly along QSL (Aulanier et al. 2006). The presence of a QSL here can be inferred by inspecting the field lines that are rooted closely in P1 but diverge largely in their south footpoints, as shown in the top panel of Figure 11. A computation of the squashing factor can further locate precisely the QSL (Savcheva et al. 2012a, 2012b), which is omitted here. This slipping reconnection is driven by the diverging motion of the new-emerging N1 and P1, which stresses the field, and results in a narrow current layer and reconnection in the QSL. For these field lines, the slipping of their footpoints from N1, a polarity getting farther away from P1 to the much nearer one, N0, is a natural result of the magnetic relaxation to a low-energy state. Due to this slipping reconnection, the final FR forms not between the newly emerged bipole P1/N1, but with its south leg rooted at the preexisting polarity N0. Such a reconfiguration further supports that the FR does not emerge bodily but forms in situ in the corona.

Flux cancellation is a basic process that transforms the double-J-shaped field lines to an S-shaped FR (van Ballegooijen & Martens 1989). Actually, the BP forms as a result of the flux cancellation, and the first appearance of BP also marks the beginning of flux-cancellation reconnection. The flux-cancellation reconnection is driven by the photospheric converging motion at the PIL. When the footpoints of two inverse J-shaped arcades are brought closer and closer to each other by convergence flows toward the PIL, reconnection between these footpoints occurs on the photosphere (see the middle panels in Figure 11). It results in a long field-line, typically of the sum length of the two J-shaped arcades, and a much shorter loop that submerges quickly, which is observed as an annihilation of inverse flux elements toward the PIL. During the reconnection, the long field-line is instantly a BPSS field line that touches the photosphere at the reconnection point (also

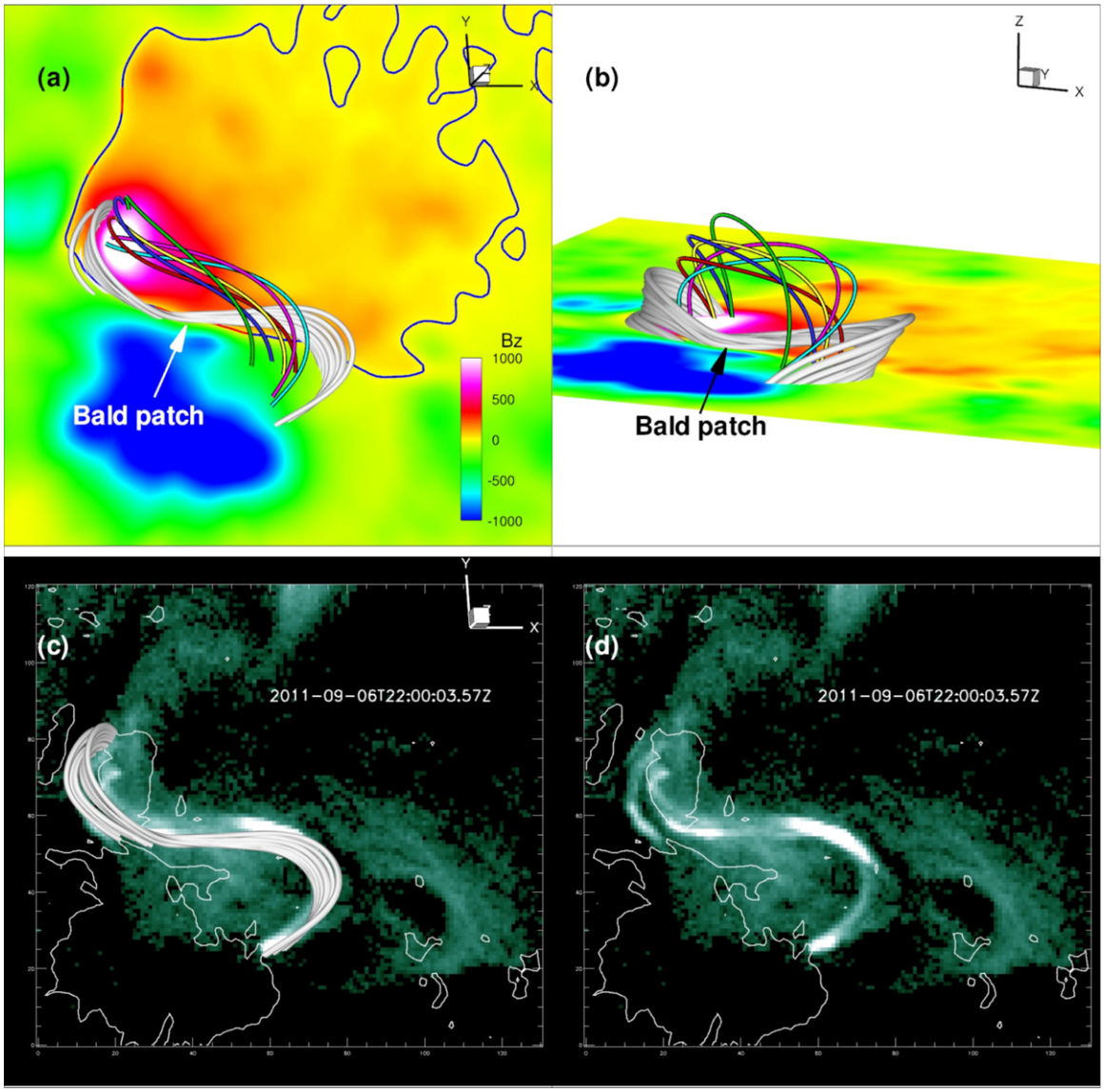

Figure 10. Observation and NLFFF reconstruction of the sigmoid field at 22:00 UT on September 6. The white thick lines are the BPSS field lines, which graze the photospheric surface at the BP. The inner body of the FR is shown by the color field lines. In particular, the yellow line is the FR axis, which is traced through the center of the helical flux in the central cross section of the FR as shown in Figure 9. The field lines are shown in both the *SDO* view (a) and a side view (b). Panels (c) and (d) are the AIA-94 image of the sigmoid, and the BPSS field lines are overlaid on the AIA observation in panel (c). Contours of ±500 G for B_z are also overlaid on the AIA images.

(A color version of this figure is available in the online journal.)

the BP point) and quickly detaches from the photosphere to be a field line inside the FR. Since the reconnection point can be considered to be on the photospheric surface, this process is also called "photospheric tether-cutting" reconnection (e.g., Aulanier et al. 2010), to distinguish it from the standard tether-cutting reconnection that occurs in the corona (Moore et al. 2001). An example of the observation in AIA-94 is shown in the left panels of Figure 12 where two J-shaped arcades merge into a single S-shaped loop. As more and more sheared arcades reconnect in this way, flux in the rope increases and the FR's axis ascends higher and higher (see Figure 9). At the same time, the length of the BP grows (see Figure 4(d)), and also the BPSS. Although the BP breaks into fragments sometimes, it persists throughout the whole formation phase and remains even through the eruption. As reconnection occurs at the BP during its whole life time, the building of the FR is conducted mainly through the flux cancellation.

It has been shown that in the case of sigmoidal FR forming in a decaying bipolar AR, the BP bifurcates, shrinks, and eventually disappears; the BPSS transforms gradually to a QSL with an HFT (i.e., a magnetic X-line-type structure) at the center; and the standard coronal tether-cutting reconnection sets in below the FR, elevating its main body off the photosphere (Aulanier et al. 2010; Savcheva et al. 2012a, 2012b). In our event, the fragmentation of the BP line does not correspond to a systematic bifurcation of the BPSS, since the BP segments do not shrink and disappear, and the FR main body is attached to the photosphere during its whole formation phase. Even though one cannot exclude the possibility of the standard tether-cutting reconnection occurring above the central part of PIL between the BP segments. The field lines near these places, as illustrated in Figure 11, resemble the configuration of the coronal tether-cutting reconnection: two inverse J-shaped arcades are sheared past each other with their arms, an S-shaped FR field line lies

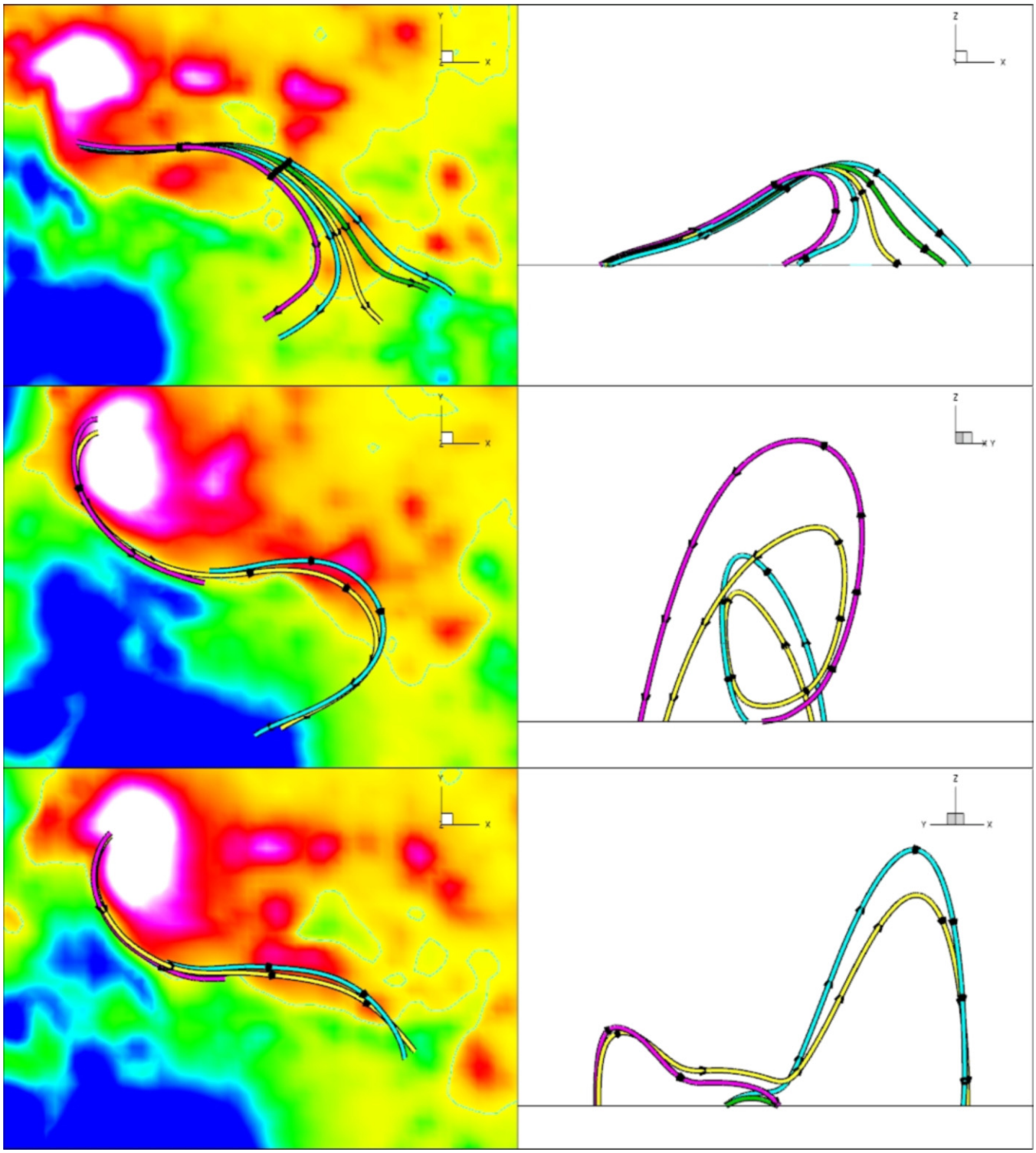

Figure 11. Illustration of different magnetic reconnections involved in the FR formation. For each panel, the field lines are selected from an NLFFF model at a given time, thus they do not represent the dynamic evolution of field lines during reconnections but help us understand how field line connectivity is changed by the reconnection. Top: the slipping type of reconnection. The field lines are rooted extremely closely in their north footpoints but diverge largely in their south footpoints as they are in a QSL. The continuous set of field lines illustrates the slipping of a single field line along the QSL, with its south footpoint moving from right to left during the reconnection. Middle: flux-cancellation reconnection. Footpoints of two inverse J-shaped field lines (the pink and cyan lines) are brought so closely toward the PIL that they connect, forming a long S-shaped field line (yellow). Bottom: coronal tether-cutting reconnection. Two inverse J-shaped arcades (pink and cyan) are sheared past each other with their arms; reconnection in the corona occurs at the closest point between their arms, resulting in a long S-shaped FR field line (yellow) and a short sheared arcade below (green). In the side views shown in the right panels the vertical axis is stretched for better visibility of different field lines.

(A color version of this figure is available in the online journal.)

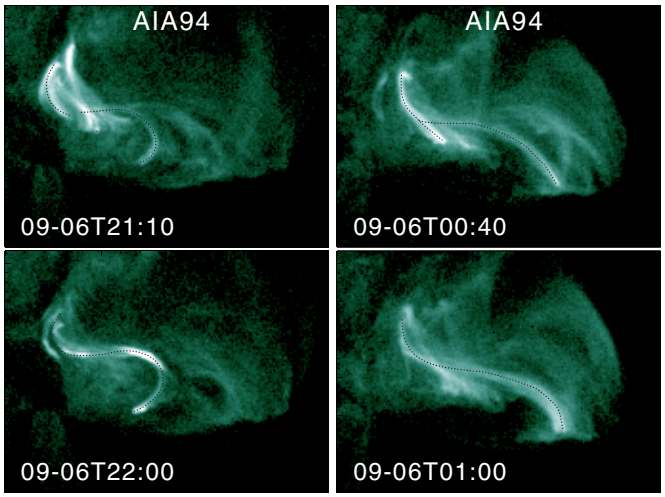

Figure 12. Left: observation of two inverse J-shaped arcades that merge at their inner footpoints into a single S-shaped loop, as in the flux cancellation cartoon. Right: observation of two inverse J-shaped arcades, which are sheared past each other with their arms, reconnecting into a long S-shaped loop, as in the coronal tether-cutting reconnection. The dashed curved lines overlaid on the images denote the loops.

(A color version of this figure is available in the online journal.)

just above them and a short sheared arcade below. In the tether-cutting reconnection, the two J-shaped arcades reconnect in the corona at the closest point between their arms above the photospheric PIL, which converts J-shaped arcades into the S-shaped field-line and forms the small arcade below the FR. In Figure 12, we also identify an observation example that agrees well with such a transition of the arcades. We thus suggest that the standard tether-cutting reconnection also contributes to the building up of the FR along with the flux cancellation.

During the buildup process, more and more flux is fed into the FR, which expands upward slowly and stretches out the envelope field, as clearly shown in Figure 9. The FR is pushed to the northwest significantly because the magnetic flux (and thus the magnetic pressure) of the south polarity N0 is much stronger than that of P1. Up until its eruption, the FR reaches a height of 14 arcsec (10 Mm) and deviates from the vertical by approximately 30°, and most flux of the FR is on the right side of the PIL as seen in the cross section. During its whole life time, the FR is attached to the photosphere at the BP, while its cross section almost develops into an inverse teardrop shape just prior to the eruption. Correspondingly, the vertical cut of the currents in the BPSS also develops from a U-shape to a nearly V-shape.

4.5. Evolution through the Eruption

A distinct release of the nonpotentiality can be seen through the eruption. Both Figures 7 and 9 show that through the eruption the helical core contracts significantly, and its envelope flux relaxes downward. As a result, the core field-lines become much shorter and thus more potential, as shown in Figure 8, and the volume current decreases and becomes more compact. Such reformation is consistent with the enhancement of the transverse field on the photosphere. Although the BP shows no substantial decrease, the BPSS shrinks significantly toward the PIL, as its long S-shaped portion disappears and a much thinner shape remains. The postflare arcades now straddle orderly over the reformed BPSS, which also indicates that a FR lies below the postflare loops. The continued presence of FR attached to the photosphere during and after eruption might be attributed to a partial expulsion of the preeruption FR (Gilbert et al. 2001; Gibson & Fan 2006). In such cases the flare reconnection occurs within the FR and breaks the FR into two parts, of which the upper part escapes while the lower part remains. We discuss this point further, along with the mechanism of the eruption.

5. INITIATION MECHANISM OF THE ERUPTION

In this section we investigate what mechanisms are involved and what roles they play in causing the eruption based on observations and coronal fields at the onset of the eruption. The magnetic field evolution of the eruption process will be analyzed in detail in the second article.

5.1. Erupting Loop

Figure 13 shows the AIA-94 observation of the early phase of the eruption. A significant brightening of the sigmoid is triggered at 22:00 UT, and the sigmoid evolves with a clear expansion of its west hook. Immediately afterward, a group of loops overlying the sigmoid (marked by arrows in the AIA-335 images) is also lit up gradually, being even brighter than the sigmoid, and expand very slightly until 22:12 UT. After that these loops accelerate rapidly toward the northwest, while they progressively faint until being invisible, and are followed by the appearance of a circular flare ribbon at about 22:17 UT. Such erupting loops have also been observed in some other sigmoid eruptions (e.g., the linear bar-like features reported by McKenzie & Canfield 2008; Green et al. 2011), but their relation with the erupting FR is not very clear. They have usually been speculated as the erupting FR itself (e.g., Moore et al. 2001; McKenzie & Canfield 2008; Liu et al. 2010; Green et al. 2011). Aulanier et al. (2010) suggest another interpretation: they are not associated with the erupting FR but with a current shell that develops within expanding field lines above the rope. In the present case, the observation of such an erupting loop is much more defined than in those previous studies. By a direct comparison with the coronal field at 22:00 UT, we can clearly identify such an erupting loop as indeed part of the FR, and in particular, it corresponds to those field lines near the rope axis (see the close resemblance between the erupting loop observed at 22:10 UT and the near-axis field lines shown in top-right panel in Figure 13). The accelerated rising of this erupting loop thus indicates the initial eruption of the FR itself, and it sheds important light on our following study of the initiation mechanism.

5.2. Magnetic Breakout versus TI

In this event, we can first exclude the KI since the twist of the FR, less than one winding of field lines, is too weak to trigger KI. Also we have not observed a clear rotation of the erupting loop (i.e., the FR axis) as it rises, which would otherwise occur in the KI of a FR. The sheared core embedded in a null-point topology resembles the lateral breakout model except that the FR has already formed before eruption. The growing magnetic pressure of the FR could cause its closely overlying flux to expand outward and stress the null-point-related separatrix, which eventually triggers the breakout reconnection. Furthermore, the quasi-circular flare ribbon supports such a null-point reconnection. However, observations of the erupting loop (Figure 13) shows that the accelerated expansion of the FR starts before

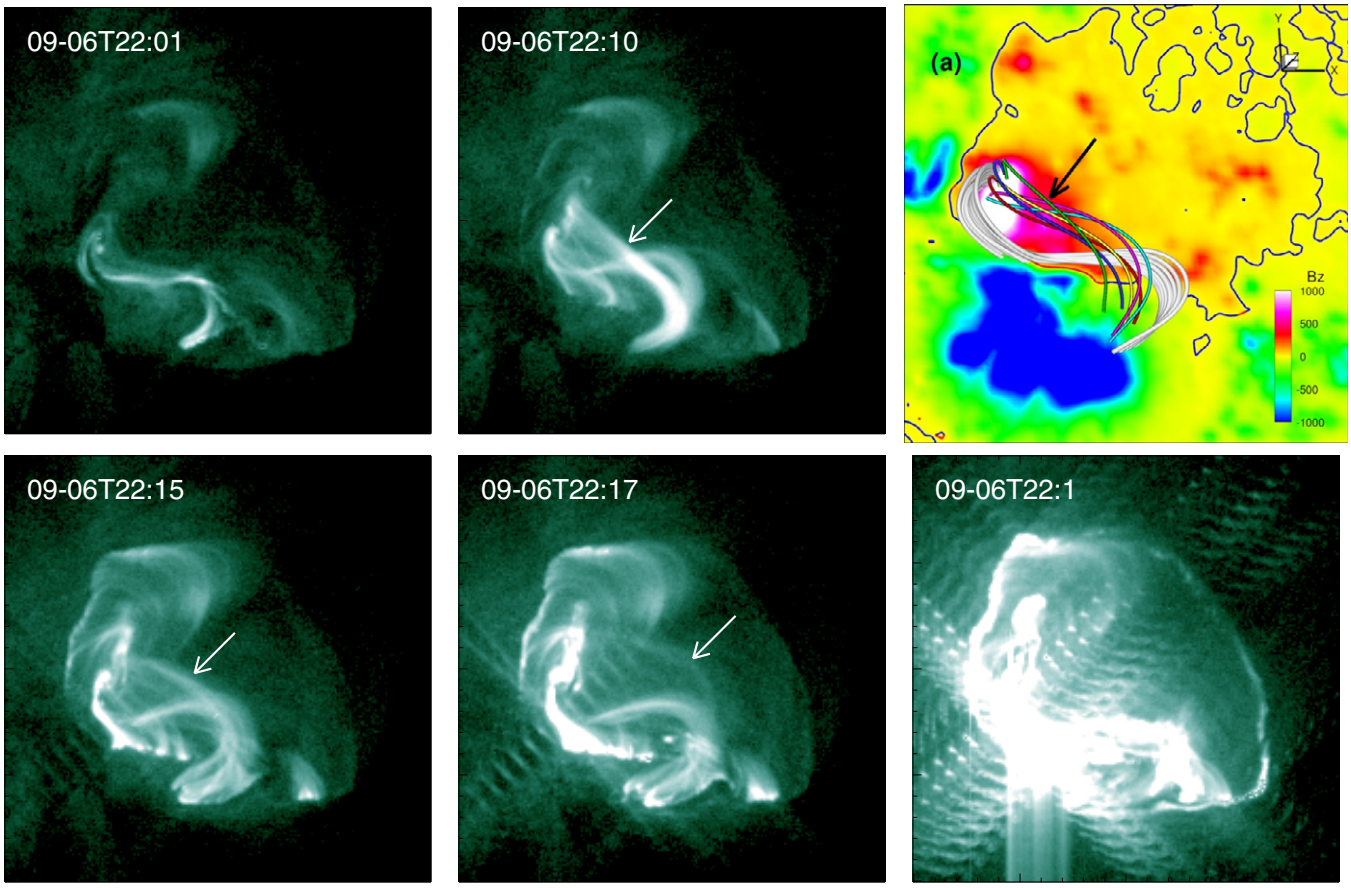

Figure 13. Observation in AIA-94 of the initiation process of the eruption. The arrows in the AIA images denote a group of erupting loops that are brightened progressively until 22:12 UT and then expand rapidly toward the northwest and become invisible after 22:17 UT. After that a remarkable circular flare ribbon appears. Panel (a) of Figure 10 is put here to compare with the observation at 22:10 UT. Although the sigmoid evolves from 22:00 UT to 22:10 UT and thus deviates slightly from the BPSS field-lines at 22:00 UT, the resemblance between the erupting loops and the field lines closely around the FR axis clearly suggests that the erupting loops correspond to those near-axis field lines.

(An animation and a color version of this figure are available in the online journal.)

the appearance of the circular ribbon, which suggests that the eruption cannot be triggered by the breakout reconnection.

The TI might apply to the FR-overlying field system of the core field because such a flux system was formed long before the breakout eruption. We note that the FR in this event does not fully develop a nearly semi-circular configuration with its main body elevated off the photosphere (except for the two legs anchored at the bottom), as in the case of a standard TI for coronal FR. Nevertheless, we can study whether the central flux of the rope reaches the domain of TI by calculating the decay index of the restraining field near the apex of the FR axis.

In the central cross section of the FR, we compute the decay index along the direction pointing from the BP to the FR axis, as illustrated in Figure 14. Since the FR stretches in this direction in the build-up phase, we show that it expands in the same direction when the TI occurs. Note that the TI only applies to the closed flux domain under the fan separatrix of the null, thus the decay index is calculated within this domain. The restraining field, also referred to as the external field, can be approximated by the potential field with the same vertical magnetogram of the NLFFF (Fan & Gibson 2007; Aulanier et al. 2010). Furthermore, because the field parallel to the rising direction actually does not contribute to the inward confining force, the decay index is computed for only the perpendicular component of the potential field (Cheng et al. 2011; Nindos et al. 2012). We then calculate the decay index

$$n(R) = -\frac{R}{B}\frac{\partial B}{\partial R}, \quad (2)$$

where R is the distance from the starting point, i.e., the BP at the bottom, and B is the perpendicular component. As plotted in the right panel of Figure 14, the decay index climbs to a critical value of 1.5 for TI (Török & Kliem 2007) at a distance of about 13 arcsec, and it stays above 1.5 for the rest of the domain. Note that the decay index does not increase monotonically but inflects near the separatrix between the closed and opened fluxes, possibly due to different variation profiles of the different flux systems. The FR axis is located at a distance of about 14 arcsec, showing that it already runs into the TI domain at 22:00 UT on September 6, a few minutes prior to the eruption onset.

In Figure 15, we plot the time evolution of $R_{\rm axis}$, i.e., the distance of the FR axis from the BP, and $R_{\rm TI}$, i.e., the critical distance for TI, during the whole day of September 6 before the eruption. With the build up of the FR, the apex of the rope axis gradually approaches the TI domain. This plot clearly shows that the eruption occurs immediately (within a few minutes) once the FR axis reaches the TI domain, which strongly suggests that the TI is the trigger mechanism of the eruption. Also, as inferred from the time profile of $R_{\rm axis}$, the FR rises very slowly with a

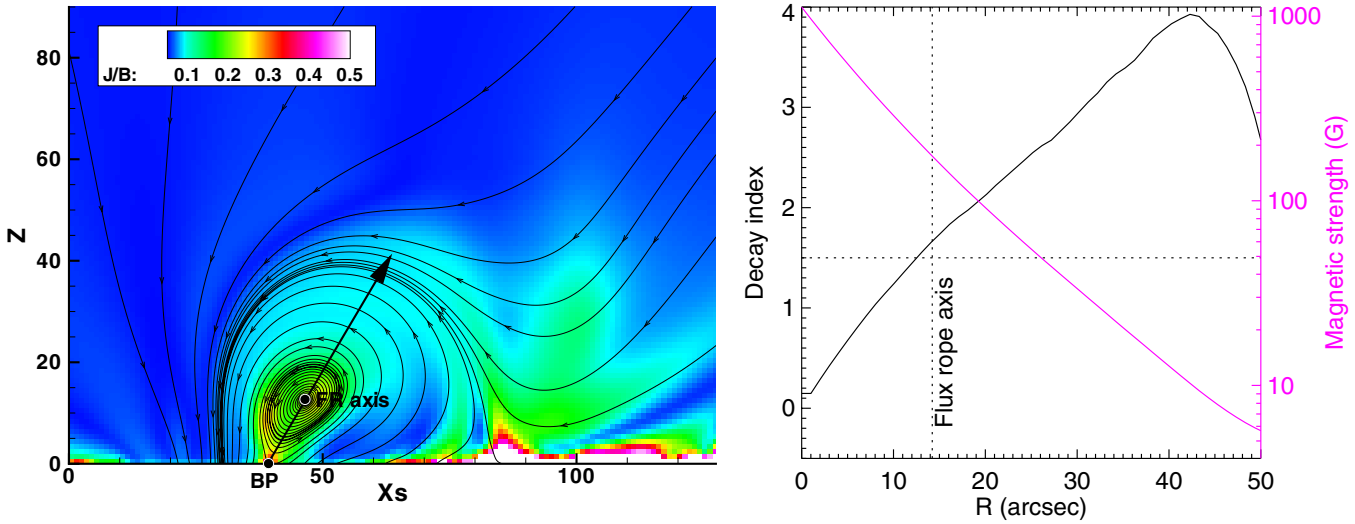

Figure 14. Left: central cross section of the core field at 22:00 UT on September 6. The background shows the current normalized by the field strength. The two black dots denote the locations of the BP and FR axes, respectively. The decay index is computed along the arrowed line pointing from the BP to the FR axis. Right: the distribution of the decay index and the strength of the restraining field with the distance R starting from the BP. The horizontal dashed line denotes a decay index of 1.5 (the critical threshold for TI), and the vertical dashed line denotes the location of the FR axis.

(A color version of this figure is available in the online journal.)

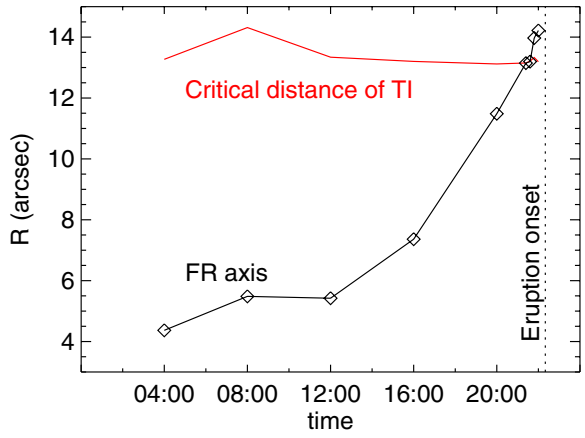

Figure 15. Time evolution for the distance from the BP to the FR axis, and the critical distance from the BP to the TI domain during the whole day of September 6. The vertical dashed line denotes the time of the eruption onset.

(A color version of this figure is available in the online journal.)

speed of a few tenths of a kilometer per second. It demonstrates the quasi-static nature of the slow buildup process of the FR, which can indeed be modeled by the static extrapolation method.

On the other hand, the critical distance of TI shows no significant variation because the potential field changes very little during the day. This is consistent with the finding of Nindos et al. (2012) that the initiation of eruptions does not depend critically on the temporal evolution of the decay index of the background field. Indeed the photospheric flux is modified very slightly by flux cancellation, being on the order of 5% (see Figure 4(a)) during the day, and also the flux distribution shows no significant variation (see Figures 5 and 8). Therefore we can further clarify that it is not the modification of the external restraining field, by lowering either its critical distance for TI or its magnetic tension force, that leads to the eruption.

Jiang et al. (2013) demonstrated the capability of reproducing the realistic solar eruptions using their data-constrained MHD model, which achieved a perfect resemblance of the simulation of the filament eruption with observations (compare Figure 1 and Figure 5 of Jiang et al. 2013). But in that article it is speculated that the null-point reconnection triggers the TI. This is because the decay index there was computed for the total magnetic field, which showed that the rope axis almost but not yet reaches the domain of TI. Also the observation of the erupting loop rising before the appearance of the circular ribbon was not noticed. We thus note that caution is needed in judging the TI using the decay index because in the realistic magnetic configuration, both the location of the FR axis and the strength of the external field are difficult to be precisely determined.

5.3. Partial Expulsion of the FR

It is still worth mentioning the short time lag of a few minutes (from about 22:00 UT to 22:12 UT) between the rapidly accelerated expansion of the FR and its entering into the TI domain. In this time interval, observations (see Figure 13) show significant brightening of the sigmoid and loops near the FR axis, but these FR loops expand very slowly, which is different from the standard TI case where the FR expands exponentially once it runs into the instability domain. The reason is possibly due to the restraining effect by the photosphere at the BP, since the instability sets in before a full detachment of the FR from the photosphere. Clearly, the flux-cancellation reconnection, which is driven by the photospheric converging motion, is a process too slow to account for the detachment of the FR in such a short time scale of minutes. As shown in the Aulanier et al. (2010) simulation, the systematic bifurcation of BP to HFT, i.e., the process of the FR detaching from the photosphere, needs hundreds of coronal Alfvén times. As a consequence, in the short time scale of eruption, the BP actually plays a role of line-tied restraint for the FR. Thus reconnection in the corona is expected to occur in order for the FR to detach from the photosphere. It is very likely that this reconnection occurs within the FR and results in a splitting of the FR (Gibson & Fan 2006). We speculate that by the combined effects of line-tying at the BP and TI-driven expansion of the upper part of the FR, the FR is torn into two portions with an X-line type reconnection formed in between. The nearly teardrop shape in the cross section of

the preeruption FR is a sign of this tearing effect. After that, the upper FR can freely expand as driven by TI. This reconnection dynamically perturbs the BPSS and results in the enhanced heating of the sigmoid and the rope. The reconnection further reforms the BPSS and also leads to a standard flare-ribbon below the upper portion of the FR. Almost at the same time, the circular ribbon appears after the moderate expansion of the FR axis. It suggests that the TI-driven expansion of the FR pushes its overlying flux quickly and triggers the breakout reconnection at the null, which produces the circular ribbon.

We summarize the scenario of the eruption as follows. The FR is built up slowly into the TI domain while the FR body still touches the photosphere; a combination of the TI-driven expansion of the FR and the line-tying at the BP results in a magnetic reconnection within the FR and thus a partial expulsion of the rope; meanwhile the TI-driven expansion of the envelope flux of the rope triggers a breakout reconnection at the null, which further facilitates the eruption. The TI is the trigger and initial driver of the eruption, and the magnetic breakout plays the role of a further driver.

6. MAGNETIC ENERGY

With the 3D coronal field, the volume energy can be computed. The energy that can be released by eruptions is the free energy $E_{\rm free}$, i.e., the total energy $E_{\rm tot}$ subtracting the potential energy $E_{\rm pot}$:

$$E_{\rm tot}=\int_V \frac{B^2}{8\pi}dV,\quad E_{\rm pot}=\int_V \frac{B_{\rm pot}^2}{8\pi}dV,\quad E_{\rm free}=E_{\rm tot}-E_{\rm pot}, \tag{3}$$

where $B_{\rm pot}$ is the potential field strength, and V denotes the core field volume that is outlined by the boxes in Figure 2 with a height of 50 arcsec. By calculations restricted within this core region, we do not consider field energy irrelevant to the eruption. Moreover most of the free energy is contained in this core region (Jiang & Feng 2013). The evolutions of these energies are plotted in panels (a) and (b) of Figure 16. As expected, the potential energy evolves in accordance with the photospheric magnetic flux, i.e., it increases mainly on the first day and then decreases episodically due to flux cancellation. The free energy increases only slightly by less than 1×10^{31} erg during the first day, but climbs rapidly on the second day of more than $\sim5\times10^{31}$ erg. This is consistent with the evolution trend of the photospheric nonpotentiality parameters, confirming that most of the free energy is built up by line-tied surface flows on the photosphere. The nonpotential energy released on early September 6 is caused by an M5.3 flare around 01:30 UT. After that the free energy increases moderately due to a small decrease of the potential energy resulting from photospheric flux cancellation, while the total energy remains almost the same. During the major flare at 22:20 UT, a step-wise drop of the total/free energy is captured by the full 12 minute cadence of the NLFFF data. After this flare, nonpotential energy is built up rapidly again due to persistent shear motions and is ready for the next eruption near the end of September 7. The abrupt loss of energy during the major flare is intrinsically related to the abrupt change of the photospheric field. The amount of free energy drop is $\sim0.4\times10^{32}$ erg, accounting for about 40% of the preflare free energy, which seems to be much lower than an estimated value of $\sim1\times10^{32}$ by Feng et al. (2013) based on the sum of flare emission and CME kinetic and potential energy for the studied event. This may be due to many reasons (Feng et al. 2013; Sun et al. 2012). One speculation is that

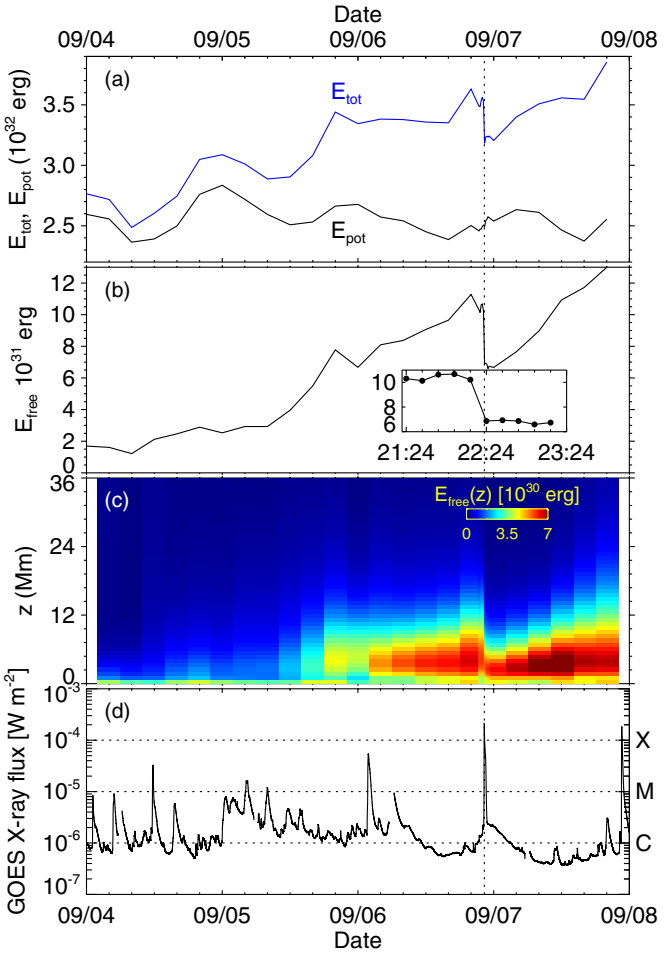

Figure 16. Evolution of magnetic energy. (a) Total magnetic energy $E_{\rm tot}$ and potential field energy $E_{\rm pot}$. (b) Magnetic free energy $E_{\rm free}$. (c) Vertical distribution of magnetic free energy $E_{\rm free}(z)$. (d) *GOES* soft-X ray flux. The inset of (b) shows the result with 2 hr around the flare peak time.

(A color version of this figure is available in the online journal.)

the NLFFF extrapolation overestimates the free energy of the postflare field, as it might be extremely dynamic and deviate from the force-free condition. In addition, the smoothing of the original magnetograms may reduce the coronal energy content by ignoring the small-scale flux elements and currents contained in the raw data. There is also a possibility that the photospheric field measurements cannot resolve even smaller field structures that carry strong currents and a nonnegligible amount of free energy.

We further study the distribution of the free energy by computing the integrations of the free energy density along three axis lines, which are, respectively,

$$\begin{aligned}E_{\rm free}(y,z)&=dy\,dz\int\frac{B^2-B_{\rm pot}^2}{8\pi}dx,\\ E_{\rm free}(x,z)&=dx\,dz\int\frac{B^2-B_{\rm pot}^2}{8\pi}dy,\\ E_{\rm free}(x,y)&=dx\,dy\int\frac{B^2-B_{\rm pot}^2}{8\pi}dz.\end{aligned} \tag{4}$$

Figure 17 shows their distributions for four snapshots. By comparing the distributions of $E_{\rm free}(x,y)$ and those of the integrated current in Figure 8, it can be clearly seen that the

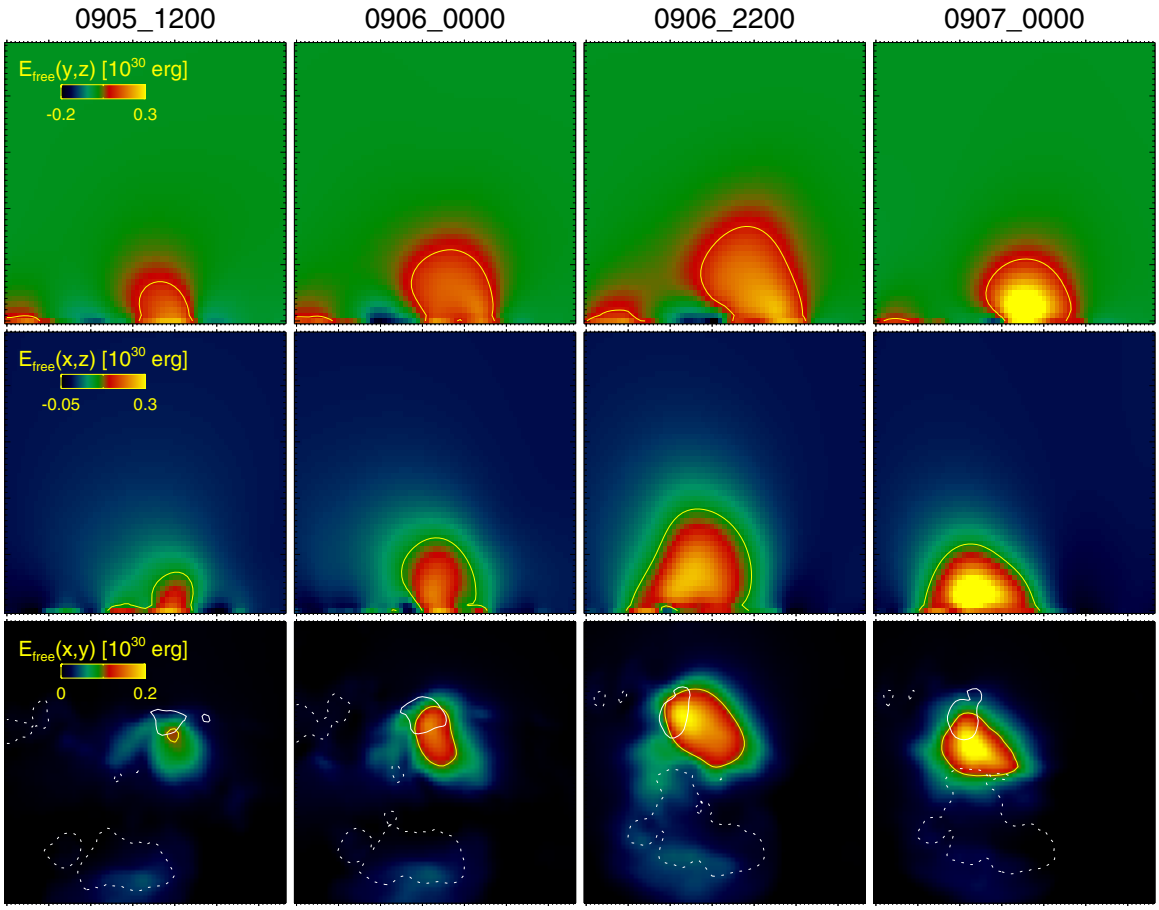

Figure 17. Evolution of the free energy distribution. From top to bottom are plots of free energy density integrated along the x, y, and z axes, respectively. Three snapshots before the eruption and one snapshot after eruption are shown. The z range for the top and middle panels is $z \in [0, 50]$ arcsec, while the x and y ranges shown in these panels are the same as those of the bottom panels. The yellow contours represent the value of 0.1×10^{30} erg, and the white contours in the bottom panels represent B_z of ± 1000 G.

(A color version of this figure is available in the online journal.)

free energy is stored largely cospatially with the current. This can be easily understood because coronal free energy is actually stored in the current-carrying field where the nonpotentiality is strong. On the other hand, the free energy generally does not concentrate within the sunspot umbras where the magnetic flux is strongest. We note that in the plots there are some small regions with negative values of integrated free energy. This is physically valid since there is no restriction that the energy density (and thus any subvolume energy) must always be greater than that of the potential field, although a nonpotential field must have a global energy content greater than that of the potential field with the same surface flux (e.g., Mackay et al. 2011).

The evolution of the free energy distribution is consistent with the evolution of the FR. The slow expansion of the FR is accompanied by the expansion of the volume with free energy and the increasing of the energy density. After the FR is partially expelled, the volume of free energy shrinks and contracts downward, abruptly and significantly. As a result, the core of its distribution becomes so compact that the density exceeds even that of the preeruption field; in spite of that the total free energy drops during the eruption. In Figure 16(c), we also plot the distribution of free energy along height z

$$E_{\rm free}(z) = dz \int \frac{B^2 - B_{\rm pot}^2}{8\pi}\, dx\, dy \qquad (5)$$

for over four days. The increasing of the height of the free-energy domain toward the major eruption can be seen. When the free energy becomes significant, it is situated mostly near the height range of 2–8 Mm. Abrupt change during the X2.1 flare also appears clearly, demonstrating a distinct downward contraction of free energy distribution from above 4 Mm to a much lower height.

7. SUMMARY

With the abundant data provided by the *Solar Dynamics Observatory* (*SDO*) and modern advanced numerical models, we have unprecedented opportunities to examine in a realistic and quantitative way many proposed mechanisms for solar eruptions, e.g., how the eruptive core field is built up, how the favorable magnetic topology is formed, and when the system runs into a unstable regime and erupts. In this article we studied a sigmoid eruption event in AR 11283 from its building up to its disruption for over three days, which involves a number of magnetic processes and thus is attractive for our study. Based on a recently developed NLFFF model (Jiang & Feng 2012, 2013), we compute a time sequence of static coronal fields to follow the slow buildup of the sigmoidal FR. As opposed to most other NLFFF methods constrained by vector magnetograms, our CESE–MHD–NLFFF code can reproduce the structure of the evolving FR very well, as is demonstrated by the perfect

matching with the observations. A detailed analysis of the fields compared with the *SDO*/AIA observations suggests the following scenario for the evolution of this region.

Within the first day, a new bipole emerges into the negative polarity of a preexisting bipolar mature AR, forming a fan-spine topology of a coronal null point on the separatrix surface between the two flux systems. In the following two days, an FR is built up slowly in the embedded core region through tether-cutting reconnections in both the photosphere (i.e., flux cancellation) and corona, which is driven by photospheric shearing, converging, and rotating flows. In this process, BPSS forms between the FR and its ambient field, and it develops into a fully S-shape. With more and more flux fed into the FR, the FR expands and the apex of the FR axis runs slowly into the TI domain near the end of the third day. However the FR does not erupt instantly as it is still attached at the bottom to the photosphere. By the combined effects of the TI-driven expansion of the FR and the line-tying at the BP, the FR is broken into two parts by reconnection within the rope. This reconnection dynamically perturbs the BPSS and results in the transient enhanced brightening of the sigmoid. Then the upper portion of the FR freely expands as it is driven by the TI, while the lower portion remains. The fast expansion of the rope pushes its envelope flux strongly outward near the null point and triggers breakout reconnection at the null, which further facilitates the eruption.

As to how a sigmoidal FR forms and erupts is still a subject of intense debate, we summarize here the important results that are concluded from the studied event but might also apply to other events with similar magnetic configurations:

1. Magnetic flux emergence into an inverse-polarity preexisting field can form a fan-spine topology configuration with a coronal null on the separatrix surface between the two flux systems (Moreno-Insertis et al. 2008; Török et al. 2009). Flare ribbons with closed circular shapes trace the footpoints of the fan separatrix and thus can usually be regarded as a signature of the presence of a null-related topology, along with the flux distribution of positive (negative) polarity surrounded by negative (positive) polarity.
2. An FR does not emerge bodily from below the photosphere, but forms gradually in the corona after the apparent new flux injection observed at the photosphere. The building up of an FR is largely driven by shear/rotation flows on the photosphere, which is possibly associated with the emergence. This is consistent with the numerical investigations of the flux emergence (Magara 2006; Fan 2009) that a twist flux tube in the convection zone cannot emerge bodily into the corona, but transports its twist by torsional Alfvén wave that manifests as the photospheric flows (Longcope & Welsch 2000).
3. Both flux cancellation (van Ballegooijen & Martens 1989) and tether-cutting (Moore et al. 2001) reconnections contribute to the in situ formation of an FR in the corona from sheared arcades, but do not trigger the eruption (Aulanier et al. 2010). Such quasi-static evolution of the FR can be characterized well by a time sequence of static NLFFF models based on continuously observed magnetograms. The result also supports store-and-release CME models with an FR existing in the corona prior to eruption, but not as a by-product of eruption.
4. Comparison of the magnetic fields with Atmospheric Imaging Assembly (AIA) observations suggests that the prominent high-temperature EUV emission is largely produced by the current sheets developing along separatrix surfaces (and QSLs) but not by the extended volume current of the FR, because the dissipation rate of the extended currents is much smaller than that of the current sheets. In particular, the sigmoid is produced by the BPSS current sheet (Titov & Démoulin 1999).
5. Although it has been shown that the TI triggers the eruption, the present case is different from that of the standard TI in which the FR is fully developed, i.e., is elevated off the photosphere away from a BPSS configuration for hours before eruption (e.g., Aulanier et al. 2010; Savcheva et al. 2012a). Here we demonstrate a case where the instability sets in before the FR is detached from the photosphere, and the photosphere can exert an additional restraining force to the FR at the BP. As a result, the FR does not erupt instantly even though its axis runs into the TI domain, and a splitting of the FR body is expected for the FR to expel partially (Gibson & Fan 2006). Unlike the finding of Fan & Gibson (2007) that the partial expulsion of an FR (i.e., there are BPSS and FR remaining below postflare loops) only occurs in the case of KI, we suggest that it can also occur in the case of TI.
6. An eruption is usually jointly produced by multiple mechanisms (e.g., Williams et al. 2005). For the studied event, in addition to the TI, the reconnection that splits the FR and the breakout reconnection that occurs at the null contribute to the final expulsion of the FR.
7. Magnetic fields experience abrupt changes through the eruption: the transverse field along the main PIL on the photosphere is enhanced. The long S-shaped BPSS shrinks significantly and reforms below the postflare arcades, which is consistent with the enhanced photospheric field, and the free energy is released mostly at a height of several Mms above the photosphere with a distinct downward compaction of its distribution. These results support the "magnetic implosion" conjecture. As a consequence, the nonpotentiality of the photospheric fields might even increase after the flare, and it is necessary to look at the 3D coronal field to disentangle these effects.

Although the basic scenario of the AR evolution has been drawn, questions remain for the dynamical evolution of the coronal field during the eruption. In particular, how does the reconnection occur within the FR, how does the BPSS evolve during this reconnection, and how is the breakout reconnection triggered? A solution to these requires an MHD simulation that is beyond the scope of this article and will be investigated in detail using the recipe given by Wu et al. (2004, 2006) in a future article of this series.

We thank the anonymous referee for helpful comments that significantly improved our manuscript. This work is jointly supported by the 973 program under grant 2012CB825601, the Chinese Academy of Sciences (KZZD-EW-01-4), the National Natural Science Foundation of China (41204126, 41231068, 41274192, 41174151, 41031066, and 41074122), and the Specialized Research Fund for State Key Laboratories. The work performed by S.T.W. is supported by NSF-AGS1153323, and Q.H. is supported by NSF SHINE AGS-1062050. Numerical calculations were completed on our SIGMA Cluster computing system. Data from observations are courtesy of NASA/*SDO* and the HMI science teams.

REFERENCES

Amari, T., Luciani, J. F., Aly, J. J., Mikic, Z., & Linker, J. 2003a, ApJ, 585, 1073
Amari, T., Luciani, J. F., Aly, J. J., Mikic, Z., & Linker, J. 2003b, ApJ, 595, 1231
Antiochos, S. K. 1987, ApJ, 312, 886
Antiochos, S. K., DeVore, C. R., & Klimchuk, J. A. 1999, ApJ, 510, 485
Aulanier, G. 2013, arXiv:1309.7329
Aulanier, G., Démoulin, P., Schmieder, B., Fang, C., & Tang, Y. H. 1998, SoPh, 183, 369
Aulanier, G., Pariat, E., Démoulin, P., & DeVore, C. R. 2006, SoPh, 238, 347
Aulanier, G., Török, T., Démoulin, P., & DeLuca, E. E. 2010, ApJ, 708, 314
Canfield, R. C., Hudson, H. S., & McKenzie, D. E. 1999, GeoRL, 26, 627
Canfield, R. C., Kazachenko, M. D., Acton, L. W., et al. 2007, ApJL, 671, L81
Chen, P. F., & Shibata, K. 2000, ApJ, 545, 524
Cheng, X., Zhang, J., Ding, M. D., Guo, Y., & Su, J. T. 2011, ApJ, 732, 87
Cheng, X., Zhang, J., Ding, M. D., et al. 2013, ApJL, 769, L25
Dai, Y., Ding, M. D., & Guo, Y. 2013, ApJL, 773, L21
Démoulin, P. 2006, AdSpR, 37, 1269
Démoulin, P. 2007, AdSpR, 39, 1367
Falconer, D. A., Moore, R. L., & Gary, G. A. 2002, ApJ, 569, 1016
Fan, Y. 2009, ApJ, 697, 1529
Fan, Y., & Gibson, S. E. 2004, ApJ, 609, 1123
Fan, Y., & Gibson, S. E. 2007, ApJ, 668, 1232
Feng, L., Wiegelmann, T., Su, Y., et al. 2013, ApJ, 765, 37
Gibson, S. E., & Fan, Y. 2006, ApJL, 637, L65
Gibson, S. E., Fan, Y., Mandrini, C., Fisher, G., & Demoulin, P. 2004, ApJ, 617, 600
Gibson, S. E., Fan, Y., Török, T., & Kliem, B. 2006, SSRv, 124, 131
Gibson, S. E., Fletcher, L., Zanna, G. D., et al. 2002, ApJ, 574, 1021
Gilbert, H. R., Holzer, T. E., Low, B. C., & Burkepile, J. T. 2001, ApJ, 549, 1221
Green, L. M., Kliem, B., Török, T., van Driel-Gesztelyi, L., & Attrill, G. D. R. 2007, SoPh, 246, 365
Green, L. M., Kliem, B., & Wallace, A. J. 2011, A&A, 526, A2
Hood, A. W., & Priest, E. R. 1981, GApFD, 17, 297
Hudson, H. S. 2000, ApJL, 531, L75
Hudson, H. S., Lemen, J. R., St. Cyr, O. C., Sterling, A. C., & Webb, D. F. 1998, GeoRL, 25, 2481
Jacobs, C., Roussev, I. I., Lugaz, N., & Poedts, S. 2009, ApJL, 695, L171
Janvier, M., Aulanier, G., Pariat, E., & Démoulin, P. 2013, A&A, 555, A77
Jiang, C., Feng, X., Fan, Y., & Xiang, C. 2011, ApJ, 727, 101
Jiang, C., Feng, X., Wu, S. T., & Hu, Q. 2012a, ApJ, 759, 85
Jiang, C., Feng, X., Wu, S. T., & Hu, Q. 2013, ApJL, 771, L30
Jiang, C., Feng, X., & Xiang, C. 2012b, ApJ, 755, 62
Jiang, C. W., & Feng, X. S. 2012, ApJ, 749, 135
Jiang, C. W., & Feng, X. S. 2013, ApJ, 769, 144
Jiang, C. W., & Feng, X. S. 2014, SoPh, 289, 63
Jiang, C. W., Feng, X. S., Zhang, J., & Zhong, D. K. 2010, SoPh, 267, 463
Kliem, B., Su, Y., van Ballegooijen, A., & DeLuca, E. 2013, arXiv:1304.6981
Kliem, B., Titov, V. S., & Török, T. 2004, A&A, 413, L23
Kliem, B., & Török, T. 2006, PhRvL, 96, 255002
Li, T., & Zhang, J. 2013a, ApJL, 770, L25
Li, T., & Zhang, J. 2013b, ApJL, 778, L29
Lin, J., Forbes, T. G., & Isenberg, P. A. 2001, JGR, 106, 25053
Linker, J. A., Mikić, Z., Lionello, R., et al. 2003, PhPl, 10, 1971
Liu, C., Deng, N., Lee, J., et al. 2013, ApJL, 778, L36
Liu, C., Deng, N., Liu, R., et al. 2012, ApJL, 745, L4
Liu, R., Liu, C., Wang, S., Deng, N., & Wang, H. 2010, ApJL, 725, L84
Longcope, D. W., & Welsch, B. T. 2000, ApJ, 545, 1089
Mackay, D. H., Green, L. M., & van Ballegooijen, A. 2011, ApJ, 729, 97
Magara, T. 2006, ApJ, 653, 1499
Masson, S., Pariat, E., Aulanier, G., & Schrijver, C. J. 2009, ApJ, 700, 559
McKenzie, D. E., & Canfield, R. C. 2008, A&A, 481, L65
Moore, R. L., & Roumeliotis, G. 1992, in IAU Colloq. 133: Eruptive Solar Flares, ed. Z. Svestka, B. V. Jackson, & M. E. Machado (Lecture Notes in Physics, Vol. 399; Berlin: Springer), 69
Moore, R. L., Sterling, A. C., Hudson, H. S., & Lemen, J. R. 2001, ApJ, 552, 833
Moreno-Insertis, F., Galsgaard, K., & Ugarte-Urra, I. 2008, ApJL, 673, L211
Nindos, A., Patsourakos, S., & Wiegelmann, T. 2012, ApJL, 748, L6
Pariat, E., Masson, S., & Aulanier, G. 2009, ApJ, 701, 1911
Petrie, G. J. D. 2012, ApJ, 759, 50
Pevtsov, A. A. 2002, SoPh, 207, 111
Régnier, S., & Canfield, R. C. 2006, A&A, 451, 319
Roussev, I. I., Lugaz, N., & Sokolov, I. V. 2007, ApJL, 668, L87
Rust, D. M., & Kumar, A. 1996, ApJL, 464, L199
Savcheva, A., & van Ballegooijen, A. 2009, ApJ, 703, 1766
Savcheva, A., van Ballegooijen, A., Aulanier, G., & DeLuca, E. 2012a, ApJ, 750, 15
Savcheva, A., van Ballegooijen, A., & DeLuca, E. 2012b, ApJ, 744, 78
Schmieder, B., & Aulanier, G. 2012, AdSpR, 49, 1598
Schmieder, B., Démoulin, P., & Aulanier, G. 2013, AdSpR, 51, 1967
Schrijver, C. J., DeRosa, M. L., Metcalf, T., et al. 2008, ApJ, 675, 1637
Seehafer, N. 1994, A&A, 284, 593
Shibata, K. 1998, Ap&SS, 264, 129
Su, Y., Surges, V., van Ballegooijen, A., DeLuca, E., & Golub, L. 2011, ApJ, 734, 53
Sun, X., Hoeksema, J. T., Liu, Y., et al. 2012, ApJ, 748, 77
Sun, X., Hoeksema, J. T., Liu, Y., et al. 2013, ApJ, 778, 139
Titov, V. S., & Démoulin, P. 1999, A&A, 351, 707
Titov, V. S., Hornig, G., & Démoulin, P. 2002, JGR, 107, 1164
Török, T., Aulanier, G., Schmieder, B., Reeves, K. K., & Golub, L. 2009, ApJ, 704, 485
Török, T., & Kliem, B. 2005, ApJL, 630, L97
Török, T., & Kliem, B. 2007, AN, 328, 743
Török, T., Kliem, B., & Titov, V. S. 2004, A&A, 413, L27
van Ballegooijen, A. A., & Martens, P. C. H. 1989, ApJ, 343, 971
Velli, M., Hood, A. W., & Einaudi, G. 1990, ApJ, 350, 428
Wang, H., & Liu, C. 2012, ApJ, 760, 101
Wang, H., Liu, C., Wang, S., et al. 2013, ApJL, 774, L24
Wang, S., Liu, C., & Wang, H. 2012, ApJL, 757, L5
Wiegelmann, T. 2008, JGRA, 113, 3
Williams, D. R., Török, T., Démoulin, P., van Driel-Gesztelyi, L., & Kliem, B. 2005, ApJL, 628, L163
Wu, S. T., & Guo, W. P. 1997, in A Self-Consistent Numerical Magnetohydrodynamic (MHD) Model of Helmet Streamer and Flux-Rope Interactions: Initiation and Propagation of Coronal Mass Ejections (CMEs), ed. N. Crooker, J. Joselyn, & J. Feynman (Geophys. Monogr. Ser., Vol. 99; Washington, DC: AGU), 83
Wu, S. T., Wang, A. H., & Falconer, D. A. 2004, in IAU Symp. 226, Coronal and Stellar Mass Ejections, ed. K. Dere, J. X. Wang, & Y. H. Yan (Cambridge: Cambridge Univ. Press), 291
Wu, S. T., Wang, A. H., Gary, G. A., et al. 2009, AdSpR, 44, 46
Wu, S. T., Wang, A. H., Liu, Y., & Hoeksema, J. T. 2006, ApJ, 652, 800
Wu, S. T., Zhang, T. X., Dryer, M., Feng, X. S., & Tan, A. 2005, SSRv, 121, 33
Zhang, J., Cheng, X., & Ding, M. D. 2012, NatCo, 3, 747